Qian Xu
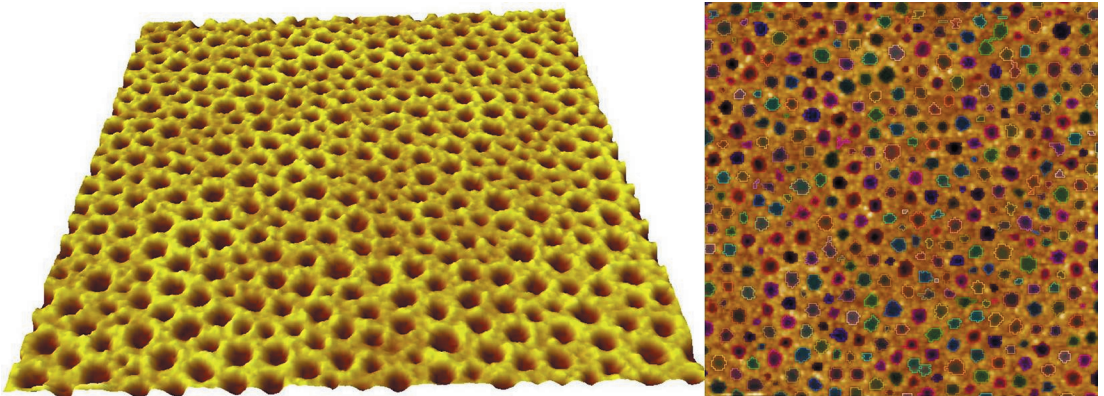
Synthesis and Characterization
of Nanoperforated Metal Oxide Thin Films

Synthesis and Characterization
of Nanoperforated Metal Oxide Thin Films

Qian Xu

Laboratory of Physical Chemistry

Center for Functional Materials

Faculty of Science and Engineering

Åbo Akademi University

Åbo, Finland, 2016

Supervised by

Professor Jouko Peltonen

Laboratory of Physical Chemistry

Åbo Akademi University, Åbo (Turku), Finland

and

Adjunct professor Jan-Henrik Smått

Laboratory of Physical Chemistry

Åbo Akademi University, Åbo (Turku), Finland

Co-supervised by

Adjunct professor Petri Ihalainen

Laboratory of Physical Chemistry

Åbo Akademi University, Åbo (Turku), Finland

Reviewed by

Doctor Tapani Viitala

Faculty of Pharmacy, Centre for Drug Research

University of Helsinki

and

Professor Galo Soler-Illia

Departamento de Química Inorgánica, Analítica y Química Física

Universidad de Buenos Aires

Opponent

Doctor Tapani Viitala

Faculty of Pharmacy, Centre for Drug Research

University of Helsinki

业精于勤，荒于嬉；行成于思，毁于随。

-韩愈

Achievements are reached by hard work rather than recreation;

Actions are done after thorough consideration rather than casual decision.

-Yu Han

PREFACE

ABSTRACT

For advanced devices in the application fields of data storage, solar cell and biosensing, one of the major challenges to achieve high efficiency is the fabrication of nanopatterned metal oxide surfaces. Such surfaces often require both precise structure at the nanometer scale and controllable patterned structure at the macro scale. Nowadays, the dominating candidates to fabricate nanopatterned surfaces are the lithographic technique and block-copolymer masks, most of which are unfortunately costly and inefficient. An alternative bottom-up approach, which involves organic/inorganic self-assembly and dip-coating deposition, has been studied intensively in recent years and has proven to be an effective technique for the fabrication of nanoperforated metal oxide thin films.

The overall objective of this work was to optimize the synthesis conditions of nanoperforated TiO_2 (NP-TiO_2) thin films, especially to be compatible with mixed metal oxide systems. Another goal was to develop fabrication and processing of NP-TiO_2 thin films towards large-scale production and seek new applications for solar cells and biosensing. Besides the traditional dip-coating and drop-casting methods, inkjet printing was used to prepare thin films of metal oxides, with the advantage of depositing the ink onto target areas, further enabling cost-effective fabrication of micro-patterned nanoperforated metal oxide thin films. The films were characterized by water contact angle determination, Atomic Force Microscopy, Scanning Electron Microscopy, X-ray Photoelectron Spectroscopy and Grazing Incidence X-Ray Diffraction.

In this study, well-ordered zinc titanate nanoperforated thin films with different Zn/Ti ratios were produced successfully with zinc precursor content up to 50 mol%, and the dominating phase was $Zn_2Ti_3O_8$. NP-TiO_2 structures were also obtained by a cost-efficient means, namely inkjet printing, at both ambient temperature and 60 °C. To further explore new biosensing applications of nanoperforated oxide thin films, inkjet printing was used for the fabrication of both continuous and patterned polymeric films onto NP-TiO_2 and perfluorinated phosphate functionalized NP-TiO_2 substrates, respectively. The NP-TiO_2 films can be also functionalized with a fluoroalkylsilane, resulting in hydrophobic surfaces on both titania and silica. The surface energy contrast in the nanoperforations can be tuned by irradiating the films with UV light, which provides ideal model systems for wettability studies.

ABSTRAKT

En av de största utmaningarna med att uppnå en hög prestanda hos avancerade anordningar inom datalagring, solceller och biosensorer är tillverkningen av nanomönstrade metalloxidytor. Sådana ytor kräver ofta både en exakt och välordnad struktur på nanoskalan samt en kontrollerbar struktur på makroskalan. I dagens läge är litografi samt schabloner framställda av block-copolymerer de mest använda sätten för att tillverka nanomönstrade ytor. Tyvärr är dessa metoder vanligen kostsamma och ineffektiva. En alternativ s.k. botten-upp-metod, som involverar organisk/oorganisk självstrukturering samt deponering med hjälp av dipcoating, har intensivt studerats under de senaste åren och har visat sig vara ett effektivt sätt att tillverka nanoperforerade metalloxidtunnfilmer med.

De övergripande målen inom detta arbete har varit att a) optimera syntesbetingelserna för nanoperforerade titaniumdioxidtunnfilmer (NP-TiO$_2$), b) att utveckla tillverkningen av NP-TiO$_2$ emot en mera storskalig produktionsprocess, samt c) söka nya användingsområden för NP-TiO$_2$, t.ex. inom solceller och biosensorer.

I denna studie har välordnade, nanoperforerade zinktitanat-tunnfilmer med olika Zn/Ti-förhållanden framgångsrikt tillverkats (med en zinkhalt upp till 50 mol-%). NP-TiO$_2$-strukturer kunde även erhållas med hjälp av bläckstråleprintning (både vid normal temperatur och vid 60 °C). För att ytterligare utforska nya biosensorapplikationer för dessa nanoperforerade metalloxidtunnfilmer, användes även bläckstråleprintning för att framställa både kontinuerliga och mönstrade polymerfilmer på rena NP-TiO$_2$-substrat samt på NP-TiO$_2$-substrat som funktionaliserats med perfluorinerade fosfater. NP-TiO$_2$-filmerna kunde också funktionaliseras med en fluoroalkylsilan, vilket resulterade i en hydrofobering av både TiO$_2$- och SiO$_2$-delarna av den nanomönstrade ytan. Genom att bestråla filmerna med UV-ljus kunde kontrasten i ytenergi mellan dessa båda delar enkelt justeras, vilket tillät att dessa filmer kunde användas som ideala modellsystem för detaljerade vätningsstudier.

LIST OF PUBLICATIONS

I. Q. Xu, J.H. Smått, J. Peltonen, P. Ihalainen, *Fabrication of nanoperforated ultrathin TiO$_2$ films by inkjet printing*. Journal of Materials Research, 30, **2015,** 2151–2160.

II. Q. Xu, M. Järn, M. Lindén, J.H. Smått, *Nanopatterned zinc titanate thin films prepared by the evaporation–induced self–assembly process*. Thin Solid Films, 531, **2013,** 222–227.

III. M. Järn, Q. Xu, M. Linden, *Wetting studies of hydrophilic–hydrophobic TiO$_2$@SiO$_2$ nanopatterns prepared by photocatalytic decomposition*. Langmuir, 26, **2010,** 11330–11336.

IV. Q. Xu, P. Ihalainen, J.H. Smått, A. Määttänen, P. Sund, C.E. Wilén, J. Peltonen, *Template–induced fabrication of nanopatterned polymeric films by inkjet printing*. Applied Surface Science, 313, **2014,** 237–242.

Author's contribution

I. The author did all the experiments and performed the AFM measurements and analysis of the results. The author wrote the manuscript.

II. The author planned all the experiments and performed the AFM and XPS measurements and analysis of the results. The author wrote the manuscript.

III. The author performed the synthesis and AFM analysis of the films.

IV. The author planned and did all the experiments and performed the AFM and XPS measurements and analysis of the results. The author wrote the manuscript.

Related publications

RI. S. Sandén, O. Sandberg, Q. Xu, J.H.Smått, G.Juška, M.Lindén, R.Österbacka, *Effect of a Large Hole Reservoir on the Charge Transport in TiO$_2$/organic Hybrid Devices*. Physical Chemistry Chemical Physics, 14, **2012,** 14186–14189.

RII. S. Sandén, O.J. Sandberg, Q. Xu, J.H. Smått, G. Juška, M. Lindén, R. Österbacka, *Influence of Equilibrium Charge Reservoir Formation on Photo Generated Charge Transport in TiO$_2$/organic Devices*. Organic Electronics, 15, **2014,** 3506–3513.

RIII. J. Puputti, Q. Xu, M. Linden, *Inhibition of Crystal Growth During Drying in Gels Derived From a Cheap, Mixed Metal Oxide Precursor*. Journal of Sol–Gel Science and Technology, 47, **2008,** 347–353.

Table of Contents

LIST OF ABBREVIATIONS AND DEFINITIONS

EISA	Evaporation-Induced Self-Assembly
AFM	Atomic Force Microscopy
SEM	Scanning Electron Microscopy
XPS	X–ray Photoelectron Spectroscopy
ESCA	Electron Spectroscopy for Chemical Analysis
GI–XRD	Grazing Incidence X–ray Diffraction
PB–b–PEO	Polybutadiene–b–Poly(ethylene oxide)
RH	Relative humidity
CA	Contact Angle
FAS	Fluoroalkylsilane
m	molar ratio
η	viscosity
γ	surface tension
ρ	density
u	withdrawal speed
θ	Contact angle
Γ	Surface energy
DOD	Drop–On–Demand
DS	Drop Spacing
Oh	The Ohnesorge number
Z	the inverse of Ohnesorge number
FFT	Fast Fourier Transformation

1. INTRODUCTION

Nanostructured metal oxide thin films of Al_2O_3, CuO, ZnO, ZrO_2, and TiO_2 (papers RI and RII), have attracted considerable attention in recent years due to their versatile properties and promising application possibilities in the fields of sensing, catalysis and solar cells.[1–5] These fast emerging application areas put tremendous demands on the morphology design of such metal oxide films. Novel top–down approaches, such as lithography[6] or nano imprinting[7] is developed to produce precise nanopatterned surfaces, which however are limited to small scale production. Bottom–up methods are economically feasible to perform with high reproducibility, which is favored for mass production. For example, the fabrication of nanoperforated TiO_2 (NP–TiO_2) thin films on various substrates through evaporation induced self–assembly (EISA)[8–9] technique, which utilizes self–organization of surfactants and metal oxide precursors upon solvent evaporation to form thin film structures, has been reported and applied during the last decade.[10–11]

The TiO_2 craters are aligned perpendicularly to the surface, which makes the substrates accessible. Faustini et al. have successfully used NP–TiO_2 thin films to deposit hard magnetic FePt nanoparticles into the nanoperforations to produce magnetic data storage devices, by a highly controlled dip-coating process from ethanol based solutions of the salt precursor.[12] The craters are evenly distributed and the diameter of the craters can be tuned between 10 to 50 nm, depending on the molecular weight of the templating surfactant, which also makes these thin films ideal for wetting studies. Fisher et al.[10] confirmed that the water contact angle measurements can be described satisfactorily by the Cassie model with this system, while Järn et al.[13] revealed that there is a shift from Cassie–Baxter to Cassie–Wenzel–type wetting when a droplet volume increased from 2 µL to 6.5 µL.

To date, the deposited area of nanoperforated oxide thin films has solely been determined by the size of the underlying substrate through the conventional dip–coating method. However, in many applications it would be more beneficial if these films could be selectively deposited onto a desired area or in the form of a pattern. Inkjet printing technology has the 'direct–write' ability to precisely deposit picoliter (pL) volumes of dispersions in well–defined patterns. It has proved to be a powerful and efficient tool for making devices such as electronics and sensors with complex patterns. Inkjet printing is a non–contact deposition method which also avoids the need for masks. Accordingly, this decreases the probability for contamination.[14]

After printing, the nanoparticles in the printed patterns of ink either dry at ambient temperature or are sintered to form a material with properties comparable to the bulk material, structurally and morphologically. Furthermore, nanoparticle materials can be added layer–by– layer to form complex 3–D structures. [15] Inkjet printing has already proven to be an inexpensive and efficient method for fabrication of silica microdot arrays up to millimeter scale, where the possibility of coupling inkjet printing to EISA of highly sensitive miniaturized sensors for heavy metal trapping and antibody detection is open. [16-17]

In Paper I, inkjet printing was successfully used as a cost–efficient means to produce NP– TiO_2 thin films at both ambient temperature and 60 °C. Millimeter–sized homogeneous NP– TiO_2 patches were obtained with similar surface structure as those of the dip–coated and drop–cast references. Nanoperforated thin films prepared by EISA have been limited to a few transition metal oxides (i.e. Al_2O_3, TiO_2 and ZrO_2). Meanwhile, nanostructured zinc titanates have shown many interesting optical and electrochemical properties and have been put to use in several important applications, including photocatalysis, non-linear optics, and as luminescent materials. [18] To combine the unique material properties and the perforation structure, nanoperforated zinc titanate thin films with different Zn/Ti ratios were produced successfully and reported in Paper II.

One important application of NP–TiO_2 thin films is to utilize the high homogeneity of the crater morphology for detailed wetting studies. In Paper III, the films were first functionalized with a fluoroalkylsilane (FAS) and then irradiated with UV light. The hydrophilic/hydrophobic contrast in the nanoperforations was tuned due to the different photocatalytic properties of titania and silica. Wetting models for heterogeneous surfaces were used to analyze the water contact angle measurements and the results were further compared to XPS data. In Paper IV, inkjet printing was used for functionalizing the NP–TiO_2 surfaces with polymeric films with similar surface morphologies. Atomic force microscopy demonstrated that the deposited polymers were evenly distributed over the substrate surface while the nanoperforated structure was maintained. These films have high potential in biosensing and electrical devices.

2. BACKGROUND

2.1 Colloidal suspensions and sol-gel processing

A colloid is defined as a suspension in which the dispersed phase is so small that gravitational forces are negligible and the interactions are dominated by short-range forces (van der Waals, electrostatic, etc.). The typical size of the particles in the dispersed phase is in the range 1-1000 nm. A sol is a colloidal suspension of solid particles in a liquid. An aerosol is a suspension of solid particles in a gas and an emulsion is a suspension of liquid droplets in another liquid.[19]

A surfactant molecule (abbreviation for surface active agent) has an amphiphilic structure and thereby the tendency to adsorb at surfaces and interfaces. The surfactants thereby lower the surface tension of liquid and solid surfaces, or the interfacial tension between two immiscible liquids. Conveniently, surfactants can be divided into ionic (anionic and cationic) and non-ionic surfactants according to the charges of the head group. In a solvent, surfactant self-assembly leads to a range of different structures in the colloidal size range, including spherical micelles, cylindrical micelles, lamellar phases, bicontinuous structures, and vesicles and so on. Thus, a surfactant suspension can often also be referred to as a sol. The first-formed aggregates are approximately spherical, which are defined as micelles. The stability of these micelles is dependent on the temperature, pH value, the solubility of the surfactant in the solvent, etc.[20]

In the sol-gel process, the starting precursors for preparing a sol typically consist of a metal or metalloid element surrounded by various ligands, e.g., $Al(NO_3)_3$ and $Si(OCH_2CH_3)_4$ where $-NO_3$ and $-OCH_2CH_3$ are ligands. Alkoxides, like $Si(OCH_2CH_3)_4$, are metalorganic compounds, but not organometallic compounds (these have direct metal-carbon bonds). Transition metal salts, e.g., $TiCl_4$, are widely used as organometallic precursors, due to the presence of highly electronegative $-OH$ groups obtained after hydrolysis in the absence of catalyst, which stabilize the metal in its highest oxidation state and render it susceptible to nucleophilic attack in the condensation reaction shown below.

$$\equiv Ti - Cl + H_2O \quad \rightleftarrows \quad \equiv Ti - OH + HCl \qquad \text{(Hydrolysis)}$$

$$\equiv Ti - OH + HO - Ti\equiv \quad \rightleftarrows \quad \equiv Ti - O - Ti\equiv + H_2O \qquad \text{(Condensation)}$$
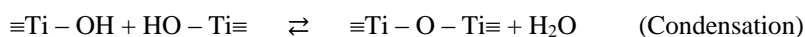
Hydrolysis is facilitated by increases in the charge density on the metal, the number of metal ions bridged by –OH or –O ligands and inhibited by increasing number of –OH ligands coordinating to the metal.[19] The typical effects of charge and pH are shown schematically in Fig. 1, where the domains of corresponding aquo, hydroxo and oxo ligands are defined. In a qualitative manner, Fig. 1 explains why the hydrolysis of lower valency cations yields aquo ligands, whereas over the same pH range, higher valency cations form oxo ligands.[21] According to the partial charge model[22], oxo ligands are good nucleophiles but poor leaving groups, while aquo ligands behave in the opposite way. In both of these two cases, condensation does not occur, since either leaving or attacking groups are missing. On the other hand, condensation is favorable for metals with intermediate valency (like Ti^{4+} and Zr^{4+}), as hydroxo ions are present at intermediate pH, which implies that both good nucleophiles (O or OH) and good leaving groups (H_2O or OH) are present in the same medium.
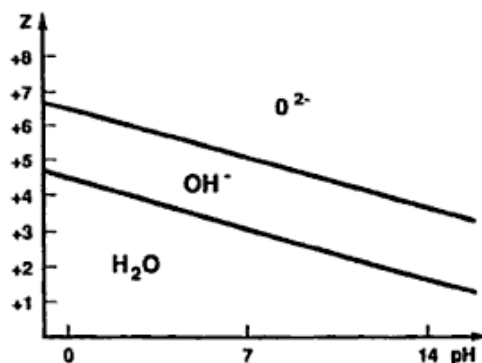
Figure 1. Charge vs. pH diagram indicating the "aquo" (H_2O), "hydroxo" (OH^-), and "oxo" (O^{2-}) domains.[21]

Colloidal particles are initially formed by condensation of the precursor molecules. The particles can link together to form larger clusters and finally the clusters can aggregate to produce a single giant cluster, which is called a gel. The non-fluid colloidal or polymer network is thus extended throughout its whole volume by a fluid phase. Gelation can occur after a sol is cast into a mold, in which case it is possible to make objects of a desired shape. Alternatively, gelation can be induced by evaporation of the solvent, as in the fabrication of films and fibers (paper RIII).

2.2 Nanopatterning techniques for metal oxide thin films

Nanopatterning techniques, including scanning probe techniques, microcontact printing, and photolithography, have emerged as the predominant methods to fabricate patterned monolayers of surfactants[23] and promising progress has been made in the last decade. For example, using scanning probe lithography, Fréchet et al. have developed a patterning methodology, which enables the patterning in a single lithography session of two different functionalities onto the same surface as separate templates for subsequent use in directed assembly.[24] Vesselin et al. have developed a method for fabrication of microparticles of bipolar surface charge distribution by microcontact printing, which works for both cationic and anionic surfactants.[25] Punit et al. demonstrated that highly fluorescent patterns can be fabricated by "photo–pens" based on photopolymerization of diacetylene films, where a range of pattern dimensions can be obtained simply by irradiating UV light through conical glass pores (10-63 μm) for different exposure times.[26] However, these top–down methods are limited by the patterning rate and the pattern size, high equipment costs, and restricted scaling up possibilities.

Various types of solution–based bottom–up approaches have been proven useful to circumvent the drawbacks of top-down nanopatterning techniques by utilizing self–assembly of molecules or nanoparticles driven by a reduction in Gibbs free energy of the system.[27–28] Recent approaches involving a careful control of the molecular interactions for designing nanopatterned surfaces include block copolymer lithography[29], colloidal templating[30], and evaporation–induced self–assembly (EISA).[8–9]

The typical principle of perforation formation is shown in Fig. 2.[31] The process consists of the preparation of the dipping sol, dip–coating, evaporation and the final thermal treatment. EISA permits the control of the final structure by adjusting both the chemical parameters (e.g., the composition of the solution and its pH) and the processing parameters (e.g., dipping speed and temperature), which makes it highly efficient. The chemical factors govern the relative quantities of surfactant and precursor as well as the sol–gel hydrolysis condensation[32–33], while the processing parameters are in charge of the diffusion of volatile EtOH and H_2O molecules to or from the film. In addition, the interplay of chemical and processing variables has been amply discussed in recent works by Soler-Illia et al.[34] For example during dip–coating, the evaporation dominates the entire film formation, which includes the composition

of the dry film and its final thickness. EISA in this case can be also described by competitive processes related to the kinetics of condensation versus the kinetics of organization, which are both influenced by the kinetics of diffusion of the volatile species. By careful control of the film deposition conditions, the EISA approach can be tuned to obtain an open monolayer structure of block copolymer micelles surrounded by the metal oxide precursor of choice, which after template removal gives a nanopatterned metal oxide surface.[10] These metal oxide thin films contain hexagonally arranged nanoperforations (or "nanocraters") with the diameter controlled, e.g., for NP-TiO$_2$, in the range of 10–50 nm by tuning the chain length of the copolymers. Another important feature of these nanopatterned structures is that the substrate is readily accessible at the bottom of the craters. This in turn allows the nanopatterned films to be selectively functionalized, making them excellent model substrates for wettability studies. However, the method is still limited to a few pure metal oxides (i.e. TiO$_2$, ZrO$_2$, and Al$_2$O$_3$) for the thinner nanocrater structures.[11] A standard preparation process for NP–TiO$_2$ thin films is described in the Materials section.
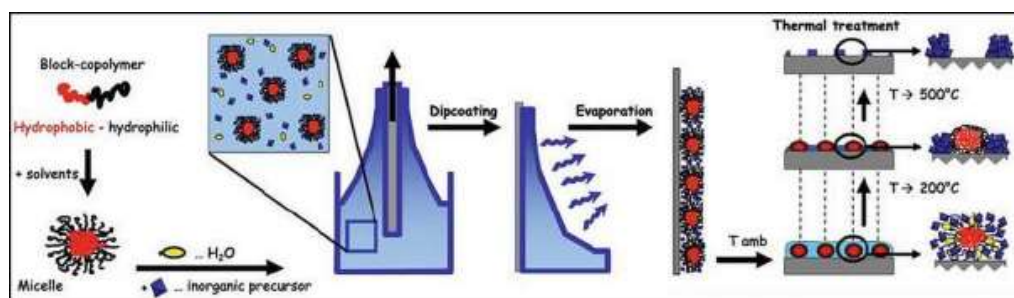
Figure 2. A scheme of fabrication of nanoperforated metal oxide thin films by EISA.[31]

2.3. Factors influencing the properties of nanoperforated metal oxide thin films fabricated by EISA

2.3.1 Chemical factors

The most effective way to tune the dimensions of perforations is to tune the structuring agent. Previous results have shown that the micelle dimension and morphology can be tuned by adjusting the solubility of the macromolecular chains in different composition of the solvents.[35] System including polystyrene-b-poly(ethylene oxide) (PS–b–PEO), hydrogenated polybutadienecoethylene-b-poly(ethylene oxide) (KLE) and polybutadiene-b-poly(ethylene oxide) (PB–b–PEO)[11] have been studied for the fabrication of nanoperforated metal oxide thin films. In the case of PS-b-PEO, the polymer is firstly dissolved in THF, EtOH is then added to

induce micellization. Different nano patterns, from disordered canyons and perforations to dispersed rings are obtained for varying amounts of EtOH in the solvent mixture. The canyons are formed due to the segregation on the substrate surface after deposition and nano-rings are formed associating to the higher dilution of the block copolymer in the solvent. In the case of KLE, the block copolymer is soluble in EtOH and THF is not needed for micellization. However, solvent polarity still plays an important role on the morphology of the final patterns. For example, when the initial solution is rich in water and poor in THF, elongated micelles are present and nano channels can be obtained after deposition.

Compared to PS–b–PEO and KLE, polybutadiene–b–poly(ethylene oxide) (PB–b–PEO), has low requirements of environmentally unfriendly solvent THF and is commercially available with many different lengths of both PB and PEO. In the case of PB–b–PEO, EtOH is a good solvent for the PEO chains, but a bad solvent for the PB chains. THF is therefore used to adjust the solubility of the whole block copolymer in a way that stable micelle formation can be obtained in the solvent. The hydrophobic PB chains are in the center part of the micelles and are thus responsible for the perforation size. The PEO chains are at the outer parts of the micelles, interacting with metal precursors, thus controlling the distance between two neighbor perforations. The different polarity induced by different EtOH/THF ratios can influence the final structure of the perforations. For example, the diameter of NP–TiO$_2$ can be tuned from 33 nm to 14 nm by replacing a fraction of EtOH with THF and reducing the proportion of water in the dipping sol. The decreased perforation diameter is related to systems with a higher dissolution capacity, which can accommodate smaller micelles with higher radius of curvature (larger contribution to the total surface energy).[31] Previous studies also revealed that the average diameter of ZrO$_2$ perforations can be tuned in the range from 9 to 67 nm.[36] Furthermore, a bimodal structure, exhibiting a homogeneous distribution of two distinct sizes of NP–TiO$_2$ (15 nm and 55 nm) in relation to the presence of two populations of micelles in the precursor solution has also been obtained.[37]

Another chemical parameter to be taken into account is the molar ratio (m) between the metal precursor and the ethylene oxide (EO) group in the solution, since the oxygen atoms present in the EO chain establish a strong coordination bond with the metal cations. Consequently, the precursor will be located in the hydrophilic and polar shell of the micelles and forms a corona, where condensation continues if an abundant amount of metal precursors exists. The detailed mechanism for the formation of nanocraters was proposed by Fisher et al. in 2006.[10] When a

too low *m* value is fixed (m<1), deposited micelles cannot be stabilized as such on the surface. The system will reduce the contribution of the surface energy by decreasing the inorganic/organic interface area through coalescence of micelles into larger copolymer domains.[31] This transformation can be considered as a spinodal phase–separation[38] taking place on the surface, which leads to organic domains bigger than micelles.

2.3.2 Processing factors

The cooling rate and aging time of the dipping sol have an influence on the final quality of the perforations. A rapid cooling down process from 70 °C to ambient temperature with a rate of 5 °C/minute can induce a broad size distribution of the craters and poor organization of the lattice. On the other hand, slow cooling rate of 1 °C/minute evidences craters with narrow size distribution.[36] The reason is that the formed micelles are not homogeneous due to the slow molecular rearrangement dynamics of long polymer chain, which need longer time to reach a more stable thermodynamic state corresponding to micelles with homogeneous size. A typical dipping sol consists of titanium–oxo–oligomers stabilized in the acidic media. The formation of larger oxo clusters and colloidal TiO_2 nanoparticles with a lower mobility may occur and the quality of crater formation can be reduced with aging time. Better organized craters are obtained with a fresh solution (within 1 week) while an aged solution (4 weeks) produces craters of lower quality. More reproducible results can be obtained by stocking the dipping sol at −20 °C and warming for 30 minutes at 70 °C before each dipping.[31]

The dip–coating speed plays an important role in the formation of nanoperforated thin films, since the thickness of such a film is in the range of a monolayer of micelles. A thicker film often relates to the multilayers of micelles which results in a mesoporous film after thermal treatment. A thinner film often leads to an incomplete surface coverage with the formation of islands of nanorings. The formation of two opposite regimes of film formation, "a capillarity regime" and "a draining regime", corresponding to slow and fast withdrawal, respectively, was recently reported.[39] For the former regime, the capillarity deposition is governed by the evaporation rate of the solvents; for the latter regime, the thickness of the liquid film (h_s) is determined by the viscous drag and the wetting properties of the liquid on the substrate surface and can be expressed by the Landau–Levich equation[40], where η_s, γ_s, and ρ_s are the viscosity, surface tension and density of the dipping solution, while u is the withdrawal speed and g is the gravitational acceleration.

$$h_S = \frac{0.94\eta_s^{2/3}}{\gamma_s^{1/6}(\rho_s g)^{1/2}}u^{2/3} \quad (1)$$

The thermal treatment has an obvious influence on the final appearance of the NP–TiO$_2$ films. A PB–b–PEO templated ZrO$_2$ system has been studied by using a technique called thermal ellipsometric analysis.[36] A consistent contraction undergoes when the temperature is increased from 25 °C to 100 °C, due to the loss of volatile solvents. From the heating range 100 °C to 200 °C, the thickness contraction is less and the system starts to consolidate due to the condensation and the consequent formation of an inorganic network. At around 200 °C, the decomposition of PB–b–PEO occurs, and at 380 °C, the crystallization of the tetragonal zirconia is suggested, after which the diffusive sintering takes place and perforations become open. The final thermal treatment at 500 °C for 5 minutes is performed to ensure an entire formation of perforations and the crystallinity of the network. Similar tendency is also obtained for a PB–b–PEO templated TiO$_2$ system.

2.4 Wetting theory

For an ideal solid surface, which is not only smooth and rigid but also chemically homogeneous, insoluble and non-reactive, the contact angle that a liquid droplet forms with the underlying solid surface is called the Young contact angle (θ_Y). The correlation between the Young contact angle and the interfacial tensions is known as the Young equation:[41]

$$\gamma_{SV} = \gamma_{LV}\cos\theta_Y + \gamma_{SL} \quad (2)$$

where γ_{SV} is the solid-vapor interfacial tension, γ_{LV} is the liquid-vapor interfacial tension, and γ_{SL} is the solid-liquid interfacial tension.

A real surface always has certain roughness and the apparent contact angle cannot express the actual Young's contact angle precisely. Based on the assumption that the liquid completely wets the grooves of a rough surface, see Fig. 3, Wenzel developed an equation (3) to relate the apparent (θ_A) and the Young's contact angle[42], where r is the ratio of the actual and projected surface areas of the sample.

$$\cos\theta_A = r\cos\theta_Y \quad (3)$$

Figure 3. A liquid droplet in the Wenzel state.

In the case of a smooth, chemically heterogeneous surface, the relationship between θ_A and θ_Y can be described by the Cassie equation.[43] A schematic picture for a solid surface representing a two-material composite is shown in Fig. 4 and the wetting is described by

$$\cos\theta_A = f_1 \cos\theta_1 + f_2 \cos\theta_2 \qquad (4)$$

where f_1 and f_2 are the area fractions of material 1 and 2, ($f_1 + f_2 = 1$), and θ_1 and θ_2 are the Young's contact angles on pure materials 1 and 2, respectively.
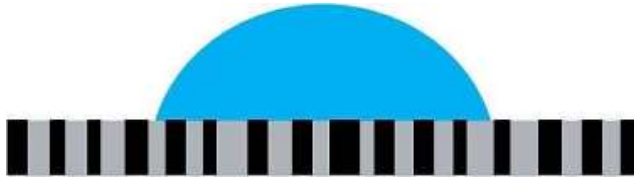
Figure 4. A liquid droplet in the Cassie state.

In the case of a hydrophobic surface, air bubbles may be trapped in the voids, resulting in a smooth composite surface of solid ($\theta_1 = \theta_S$) and vapor ($\theta_2 = \theta_V = 180°$), see Fig. 5. The Cassie equation can be then written

$$\cos\theta_A = f_s \cos\theta_s + f_s - 1 \quad , \quad (5)$$

where f_s is the fraction of solid material and θ_S is the contact angle of liquid on that solid material. This model is referred to as the Cassie-Baxter equation.[44]
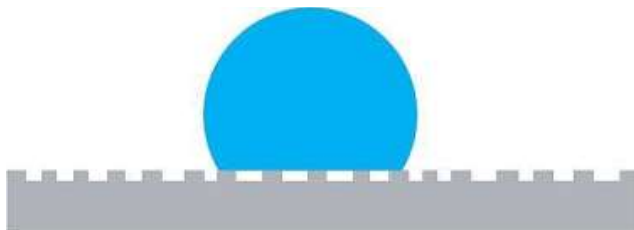
Figure 5. A liquid droplet on a hydrophobic surface.

If the chemical heterogeneities are not in the form of discrete patches but are of molecular or atomic dimensions, the Israelachvili equation[45] has been suggested to describe the wetting as follows:

$$(1 + \cos \theta_A)^2 = f_1 (1 + \cos \theta_1)^2 + f_2 (1 + \cos \theta_2)^2 \qquad (6)$$

2.5 Inkjet printing and ink formulation

There are four techniques to bring about ejection of droplets from a print head: thermal, piezoelectric, electrostatic and acoustic. However, the most common inkjet printers are often based on either drop–on–demand (DOD) thermal or piezoelectric print heads.[46] A schematic DOD piezoelectric inkjet printing system is shown in Fig. 6. In the print head, by tuning the voltage, the deformable piezocrystal responses to the electrical driving signal, and the deformation of the membrane causes a pressure impulse to the ink chamber, expelling a single droplet from the orifice. The number of droplets printed on the substrate for one jet can be tuned by the number of working nozzles. The chamber is refilled through the inlet by capillary force at the orifice. The platform under the substrate can move flexibly in both X and Y directions and the distance between the nozzle head and the substrate is also adjustable. The overall settings make it possible to print patterns with desired material amount.
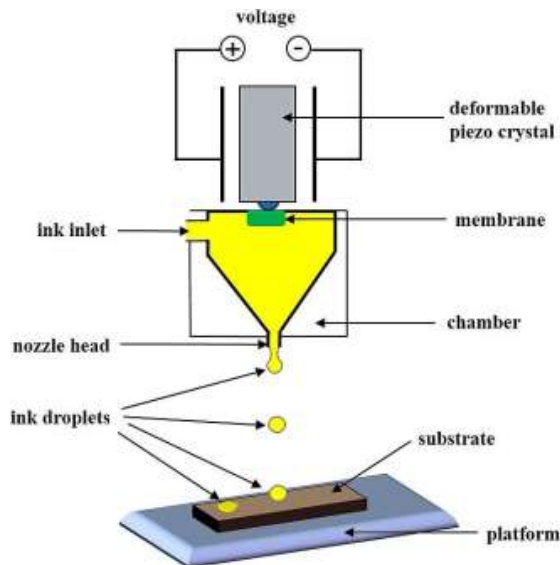
Figure 6. A Scheme of a DOD piezoelectric inkjet printing system.

It is essential to understand how printing parameters and/or ink properties affect the deposition quality. The Ohnesorge number (*Oh*), which is written in terms of the square root

of the Weber number divided by the Reynolds number [47], can be used to estimate the printability of the liquids. Fromm[48] used the Z number, the inverse of Ohnesorge number, grouping of fluid properties to provide a dimensionless analysis of the mechanics of droplet formation in a DOD piezoelectric print head:

$$Oh^{-1} = Z = \frac{\sqrt{d\rho\gamma}}{\eta} \quad (7)$$

Here, d is the diameter of the nozzle aperture, ρ, γ and η are the density, surface tension and viscosity of the liquid, respectively. If the Z value is too small, e.g., with a large viscosity, the viscous dissipation within the fluid prevents droplet formation and a large pressure pulse is required to eject a droplet; if the Z value is too large, e.g., with a high surface tension, the balance between surface tension and viscosity results in the jet of fluid breaking into a series of satellite droplets. Fromm predicted that drop formation in DOD systems was only possible when Z > 2 and that for a given pressure pulse, the droplet volume increases as the value of Z increases. This result was also supported by Jang et al., who determined experimentally the suitable printability range when 4 < Z < 14.[49] However, Meixner et al.[50] defined it to be 1 < Z < 10 for a successful printing of polymer inks and Derby et al. proposed DOD printing can take place in the same range 1 < Z < 10 for wax–based alumina suspensions, where the lower limit is determined by the dispersion's viscosity dissipating the pressure pulse and the upper limit represents the formation of satellite droplets rather than a single droplet.[51–52] In practice, a system where Z is much larger than 10 is still printable as long as the satellites can merge with the main droplet. Schubert et al.[53] summarized that a number of common solvents with low viscosity from 0.4 to 2 mPas could be still printed (the Z numbers thus varied from 21 to 91).

When inkjet-printing suspensions, the particle size is an important parameter that must be controlled in order to avoid the clogging of the print nozzle. Therefore the size of the particles as well as the colloidal stability of the sol must be carefully controlled. A useful rule of thumb is to keep the particle size down to ca 1% of the nozzle diameter in order to minimize the risk of clogging.[54]

As a tool for industrial manufacture, a number of functional polymers have been successfully inkjet printed for different applications, such as polymer light-emitting diode displays and

liquid–crystal display color filters, organic electronic components and sensors.[55–56] The printing of metal particles is attractive and already shows great potential e.g., to obtain low temperature 3D metal micro-structures[57], to fabricate thin film transistors with high field–effect mobility based on indium zinc tin oxide[58], as well as to improve magnetic data storage by incorporating nanoparticles of iron oxide [(Fe_2O_3, γ–Fe_2O_3) and Fe_3O_4].[59]

3. AIMS AND OBJECTIVES

Nanoperforated metal oxide thin films of ZrO_2 and TiO_2 have attracted considerable attention due to their versatile properties and promising application possibilities in the fields of catalysis, data storage, sensing and solar cells. The overall objective of this work is to explore new functionalities, improve fabrication conditions and methods, as well as to seek for new applications for NP-TiO_2 thin films. The objectives are summarized in Fig. 7 and they are as follows:

I.   To develop cost-effective fabrication methods of NP-TiO_2 thin films which enable preparation of patterned structures and provide the possibility for scaling up the production

II.   To optimize the synthesis conditions of nanoperforated mixed metal oxide systems, e.g., zinc titanate thin films, which have interesting optical and electrochemical properties with potential applications in photocatalysis and energy storage (batteries).

III. To use the nanopatterned metal oxide films with tunable surface energy as a platform for systematic wetting studies

IV.   To utilize the morphology of NP-TiO_2 for the fabrication of nanoperforated polymeric thin films
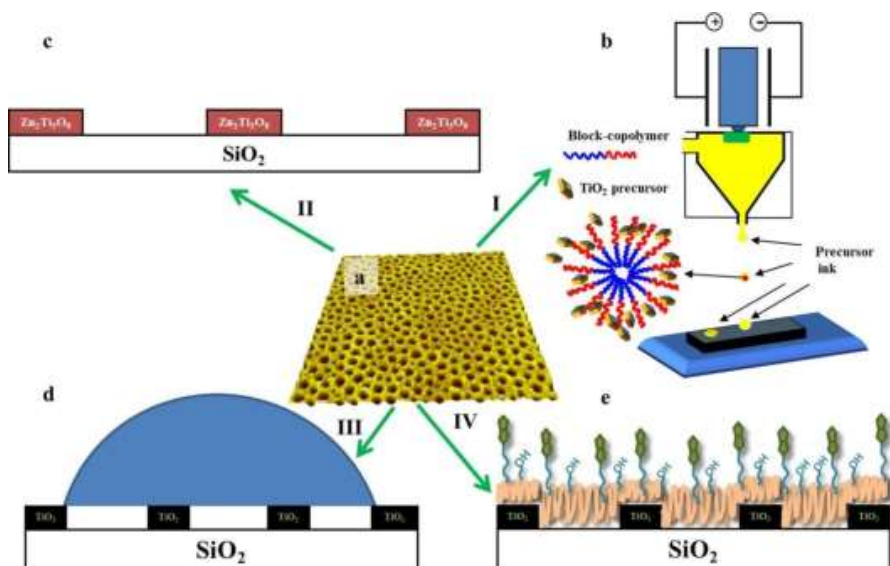
Figure 7. The objectives of this study: a) AFM topographic image of NP–TiO$_2$ fabricated by dip-coating, and b) a scheme for NP–TiO$_2$ fabrication by inkjet printing, c) NP zinc titanate fabrication by dip-coating, d) wetting studies on NP–TiO$_2$ films and e) biotinylated polythiophene derivative inkjet–printed onto NP–TiO$_2$.

4. MATERIALS AND METHODS

4.1 Materials

4.1.1 Substrates

Pieces of smooth silicon wafers (MEMC Electronic Materials, S.p.A.) were treated in a 3 M HNO$_3$ aqueous solution for 24 h, after which they were rinsed with distilled water and ethanol and stored in purified (Milli–Q) water. Just before deposition, the wafers were removed from water, rinsed with ethanol and acetone.

4.1.2 Surfactants

To obtain TiO$_2$ layers with nanoperforations, a PB–b–PEO block copolymer (polybutadiene–b–poly(ethylene oxide), P2325–BdEO, MW$_{PB}$ = 32000 g/mol, MW$_{PEO}$ = 43500 g/mol) purchased from Polymer Source Inc. was used as the main templating agent. PB–b–PEO block copolymers can form a micelle structure of a hydrophobic PB core and a hydrophilic flexible PEO shell in the solvents.

4.1.3 Polymers and ink formulations

The synthesis of biotinylated polythiophene derivative (PBTL) has been described by Ihalainen et al.[60] In short, biotin-functionalized tetraethylene-glycol thiophene (82 mg) and tetraethylene-glycol thiophene (397 mg) was dissolved in 12 ml dioxane under argon. $FeCl_3$ (781 mg) was added and the mixture was stirred at 40 °C overnight. The mixture was diluted with 10 ml of a solution of 0.2 M EDTA + 0.5 M Na_2SO_3, filtered and purified by dialysis (Aldrich D7884 MWCO 2000, benzoylated) for five days, yielding a PBTL solution of 6.8 mg polymer /ml. This was dissolved in water:ethyleneglycol (volume ratio 70:30) producing a 4.8 mg/ml PBTL ink solution.

The synthesis of Dinonylnaphthalene sulfonic acid-doped polyaniline (PANI-DNNSA) has been described by Kinlen et al.[61] In short, one tenth of a mole of DNNSA (as a 50% w/w solution in 2-butoxyethanol) was mixed with 0.06 mol of aniline and 200 ml of water to form an emulsion, which was chilled to 5 °C, stirred, and blanketed with nitrogen. Ammonium peroxydisulfate (0.074 mol in 40 ml of water) was added dropwise to the mixture over a period of approximately 1 hour. The reaction was allowed to proceed for 17 hours, during which time the emulsion separated into a green 2-butoxyethanol phase and a colorless aqueous phase. The organic phase was washed three times with 100 ml portions of water, leaving a dark green, highly concentrated polyaniline phase in 2-butoxyethanol, which was dissolved in xylene to produce a 1 wt% PANI-DNNSA ink solution.

4.1.4 Dipping sol

The $TiCl_4$ precursor was prepared by mixing 0.1 mol of $TiCl_4$ (>99%, Fluka) and 0.5 mol of EtOH in the fume hood and cooling down for at least 3 hours. The $ZnCl_2$ precursor was prepared by dissolving 1.36 g $ZnCl_2$ (>97%, Sigma) in 10 ml of distilled water.

An overview of the standard preparation steps of the dipping sol can be described as following: (a) 0.02 g PB–b–PEO is firstly dissolved in 3.4 ml THF and then 5.0 ml of EtOH is added, this solution is annealed at 60°C for 5 minutes until the solution becomes transparent. This solution is called solution A. After cooling down, the solution is treated by ultrasonication to ensure a complete dissolution of the PB–b–PEO. (b) $TiCl_4$ precursor is mixed with 0.2 ml Milli–Q water and 2.5 ml EtOH for 45 minutes. This solution is called solution B. (c) Solution A is mixed with solution B (forming the dipping sol) which is treated by ultrasonication to ensure a homogeneous mixture. The inorganic Ti–oxo clusters will

interact with the PEO shell, since the polar PEO units are hydrophilic, which can form coordination bonds with Ti^{4+} center through the interaction between the free electron pairs of O atoms and the vacant d–orbital of the metallic atoms. Here, in the final dipping sol, the molar ratio between $TiCl_4$, PB–b–PEO, EtOH, THF and Milli–Q water was kept constant at 1:0.0006:274:88:23, while the metal chloride composition $(TiCl_4)_{1-x}+(ZnCl_2)_x$ was varied (x = 0, 0.1, 0.25, 0.5, 0.75 and 1, respectively).

4.2 Processing methods

4.2.1 Dip coating

The solutions were deposited on cleaned silicon wafers in two different ways: the first method was dip coating, which was performed by a KSV Dip Coater DC (KSV Instruments Ltd., Helsinki, Finland), shown schematically in Fig. 8. The withdrawal rate was kept constant at 1.2 mm/s with a relative humidity (RH) of less than 20 % at ambient temperature (23 ± 2 °C).
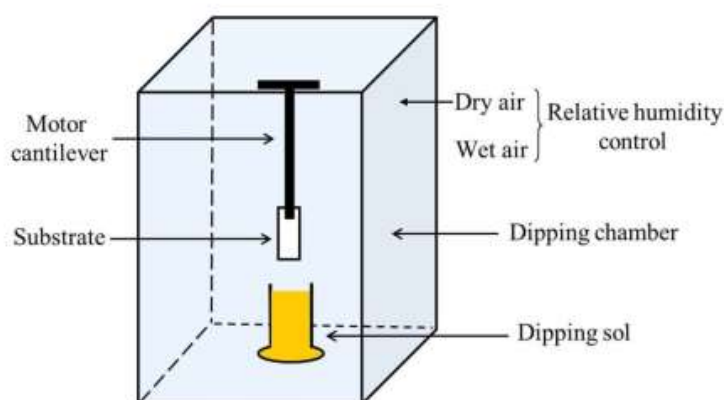
Figure 8. A scheme of a dip–coater.

4.2.2 Inkjet printing

The second method was inkjet printing, which was performed with a Dimatix Materials Printer (DMP–2800, FUJIFILM Dimatix Inc., Santa Clara, USA). The nominal droplet volume was 10 pL, while a 27 ± 3 V firing voltage and a custom waveform were used to ensure optimal droplet formation, with a jetting frequency of 3 kHz. The print pattern was designed with Microsoft®Paint (Version 5.1) software to allow simultaneous printing with varying print amount by using different drop spacing (DS 5–200 µm).

16

The polymers printing was done under ambient conditions using a single nozzle (with a diameter of 21.5 μm) and the samples were left to dry in ambient air after printing. The precursor ink was printed under ambient conditions without and with plate-heating (60 °C), using either a single nozzle or 16 nozzles open simultaneously. The samples were left to dry at ambient temperature after printing, then sintered at 500 °C for 10 min.

4.3 Surface modification methods

In order to selectively functionalize the $NP–TiO_2$ substrates, the continuous TiO_2 network was modified by immersing the films in a 1 wt–% aqueous solution of Zonyl FSE (Dupont, Wilmington, USA) for 5.5 hours, shown in Fig. 9 a. The phosphate group was able to bind selectively only on the TiO_2 surface, resulting in a hydrophobic TiO_2 and hydrophilic SiO_2 surface after modification. This film had a static water contact angle value of 90º.

FAS, $CF_3(CF_2)_5(CH_2)_2Si(OC_2H_5)_3$ (Sigma–Aldrich, 98%), was attached to the $NP–TiO_2$ films by chemical vapor deposition, shown in Fig. 9 b. At 70 ºC, self–assembled FAS monolayers on the overall film were formed by placing clean pieces of $NP–TiO_2$ films in poly–ethylene tubes with 100 μL of FAS solution for 20 hours, as the $–Si(OC_2H_5)_3$ group can bind on both TiO_2 and SiO_2 surfaces. After functionalization, the films were rinsed thoroughly with Milli–Q water. The FAS functionalization of the TiO_2 and SiO_2 reference films was done in the same way. In the following step, the FAS–functionalized films were irradiated with UV light (λ=254 nm) at a working distance of 6 cm in air under different periods of time. Under UV irradiation, the monolayers on TiO_2 surfaces were decomposed much faster than those on SiO_2, which was explained by the different photocatalytic properties of TiO_2 and SiO_2, thus leaving a hydrophilic siloxane headgroup surface on TiO_2 and a hydrophobic FAS surface on SiO_2.
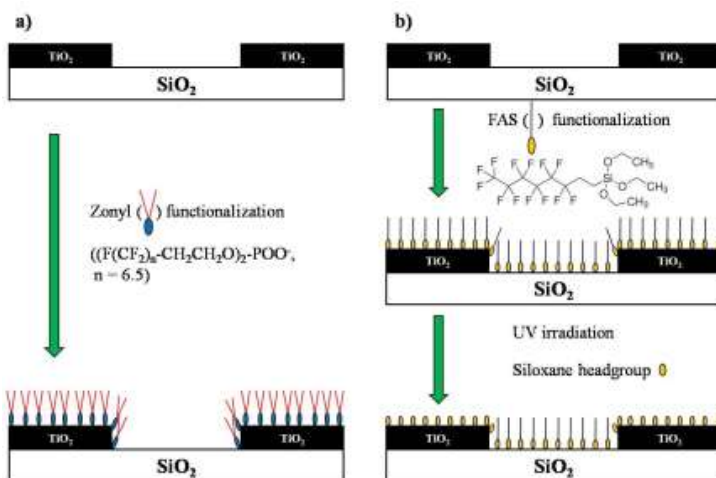
Figure 9. Surface modification of the NP–TiO$_2$ substrates with a) Zonyl and b) FAS.

5. CHARACTERIZATION

5.1 Surface tension and surface energy measurements

The surface tension of a liquid can be measured by the maximum bubble pressure method, which is based on the measurement of the pressure in a bubble growing at the tip of a capillary immersed into the target liquid. When a bubble grows at the tip of a capillary, the bubble pressure rises at a decreasing bubble radius, the pressure rises to the maximum value at the point, where the bubble forms a hemisphere and achieves its smallest radius. After the bubble passes this maximum pressure it grows quickly, separates from the capillary and a new bubble is formed. The surface tension is calculated via the Young–Laplace equation taking the capillary radius as the radius of curvature:

$$P_{max} = {2\gamma}/{R} \qquad (8)$$

Here γ is the surface tension of the liquid and R is the capillary radius. The surface tension of the solutions in this thesis was determined by a SensaDyne PC9000 surface tensiometer (SensaDyne Instrument Division, Mesa, USA) at 20 °C.

A CAM200 contact angle goniometer (KSV Instruments Ltd., Helsinki, Finland) was used for the determination of water contact angles. Typically, a 2 μL droplet was deposited on the surface under study with a syringe needle. The static contact angle was obtained at the point where drop length and volume remained constant. The liquid was then added to or removed from the droplet, and the advancing/receding contact angle was determined just when the

liquid front was to expand/retract, respectively. The contact angles were calculated using the software supplied with the instrument. The results are given as mean values from 3 to 5 measurements, with a standard deviation of less than 3°.

The Owens–Wendt method[62], where the total surface energy (γ_s) is determined as the sum of the polar (γ_s^p) and dispersive (γ_s^d) components, was used for the surface energy determination. The measurements of contact angles of water, ethylene glycol (EG) and diiodomethane (DIM) on the substrates in ambient conditions were performed and the values of the surface tension components suggested by van Oss et al.[63–64] were used for the probe liquids.

5.2 Surface morphology

5.2.1 Atomic Force Microscopy (AFM)

AFM, firstly introduced by Binnig et al. in 1986[65], is nowadays the dominating technique within the family of scanning probe microscopes (SPM). AFM is based on measuring tip–surface interaction forces in contrast to its precursor, a Scanning Tunneling Microscope (STM)[66], which is limited to the analysis of conducting or semiconducting samples.

There are three primary imaging modes in AFM: the contact mode, the tapping mode and the non–contact mode.[67] However, the non–contact mode is hardly used anymore in modern AFM instruments, due to the obtained low resolution. In contact mode, the cantilever deflection is usually kept constant during scanning. A change in cantilever deflection due to height differences on the sample surface can be compensated by a corresponding change in the z–piezo position by a feedback loop between the z–piezo and the photodiode, which provides the height information during an x-y scan, thereby generating 3D image of the surface. The contact mode is suitable for rough and hard surfaces but it can damage soft sample surfaces. In tapping mode, the cantilever is driven to oscillate at its own resonance frequency and the tip taps the surface lightly during scanning. A constant tip–sample interaction is maintained by maintaining constant oscillation amplitude, and thus a surface image can be obtained during X–Y scanning. Tapping mode can provide high resolution for soft surfaces. In addition, the phase angle of an oscillating tip can be recorded during scanning. The phase angle (phase shift) is proportional to tip-sample adhesional forces and

viscoelastic interactions, thereby phase contrast imaging can yield information about phase separation and structural grain boundaries on the studied surface.
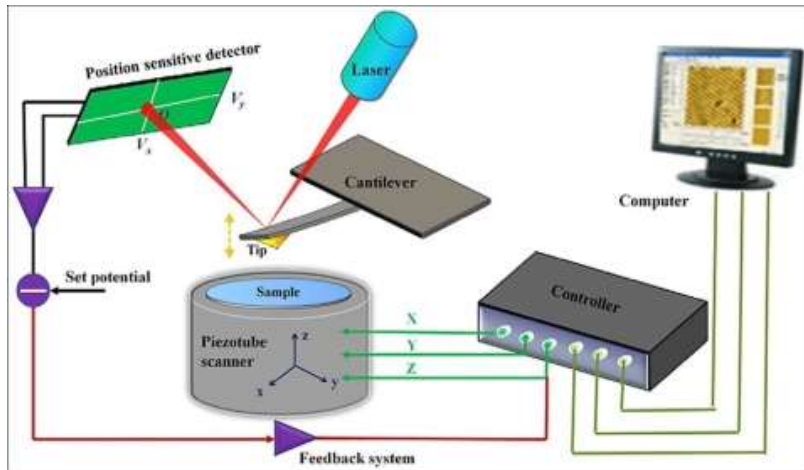
Figure 10. A schematic presentation of an AFM.[68]

Fig. 10 shows a schematic presentation of the components of an AFM.[68] Typically, a sharp tip with a radius of curvature of a few nanometers is attached to a flexible silicon or silicon nitride cantilever. While the tip is oscillating and probing the surface, the sample is accurately moved by a piezoelectric scanner in x, y and z directions. The repulsive/attractive forces between the tip and the sample cause bending of the cantilever, i.e. the cantilever acts as a force sensor. The cantilever deflection is monitored by focusing a laser at the end of the cantilever from where it is reflected to the position sensitive detector (photodiode). The oscillation amplitude can be kept constant during scanning by adjusting the sample position in z direction with the help of a feedback loop between the piezoelectric scanner and the photodiode. The changes in the phase angle of the oscillating tip at different positions of the sample provide additional information about the tip–sample interactions such as adhesion and viscoelasticity. The samples in this thesis were all calcinated at 500°C (except further caption) before AFM characterization, which were continuous smooth and hard surfaces of TiO_2 nanoperforations on Si-wafers, thus make AFM an ideal tool for characterizing the surface morphology with high resolution.

Since the introduction of tapping mode, the most significant scientific breakthrough in AFM technology is Peak Force Tapping. In this mode, the interaction force is measured directly by

the deflection of the cantilever on pico-Newton level. The tip shape and sample integrity can be well maintained by this superior force control, enabling the imaging with very small forces. With this imaging mode measurements of even the smallest biological structures, such as double helix DNA can be carried out.[69]

Due to the fact that the tips used in AFM imaging are not ideally sharp, an AFM image does not always correspond precisely to the true dimensions of the imaged objects. The dimensions may be somewhat distorted due to the tip–sample convolution effect, see Fig. 11. The convolution does not often influence the height of a feature but rather the lateral dimensions. Tips with high aspect ratio can provide better resolution.

Efforts have been made to improve deconvolution and increase the accuracy of AFM measurements. Markiewicz et al.[70] presented a simple algorithm to separate out the tip and sample in the images obtained by AFM, which provides a way of visualizing the probe tip in a nondestructive manner. It enables the deconvolution of the probe tip from the image, resulting in a more accurate picture of the sample. Bukharaev et al.[71] reported another deconvolution algorithm, which can be used for reconstructing a more accurate AFM image. From the AFM image profile, with the inverted tip located at a constant height, the offered numerical deconvolution method is easy for concrete practical realization. Canet-Ferrer et al.[72] proposed a method to study the influence of the size, shape and aspect ratio of different nanometric motifs on a flat substrate. They concluded that the convolution artifacts can be extended to any kind of motif including real surface roughness and in most cases the real motif's width can be estimated from AFM images without knowing its shape in detail.
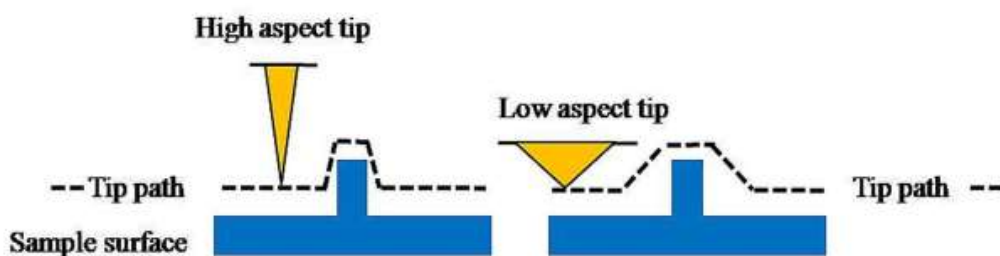
Figure 11. A scheme of tip–sample convolution.

AFM images in this thesis were captured using a Nanoscope V instrument (Veeco Metrology Group, Santa Barbara, CA). All the images were recorded in tapping mode under ambient

conditions (RH = 23 ± 3%, T = 23 ± 2°C) using silicon cantilevers (NSG 10, NT–MDT, Russia) with a resonance frequency between 190 and 325 kHz, and a nominal radius of 10 nm. All the images were analyzed by the Scanning Probe Image Processor software, SPIP 5.1.3 (Image Metrology, Denmark).

The Particle and Pore Analysis module was used for the detection and analysis of the crater structures in this study, which can be shown as colored areas each surrounded by a contour line. A vast number of geometrical parameters can be calculated. For a typical NP-TiO$_2$ thin film, the extracted nanocrater size and wall thickness were about 30 nm and 25 nm, respectively. The Nearest Neighbor Distance of the craters was found to be 57 nm, describing the distance between the geometric centers of the crater and its nearest neighbor and can be used to calculate the repeating unit distance in the pseudohexagonal pattern. This value (57 nm) corresponds well to the value obtained by adding the nanocrater size and wall thickness together (~55 nm). Roundness describes the shape's resemblance to a circle (it will approach 1.0 the closer the shape resembles a circle). Furthermore, a parameter called Material Volume can be estimated from the height histogram (Paper I). Since the silicon wafer substrate is accessible through the nanoperforations, the AFM height images can directly be used to estimate the thickness of the deposited metal oxide layer. For the pure TiO$_2$ layer, the estimated height is about 2 nm.

The Fourier transform is a powerful tool for image analysis, in particular for the analysis of repeated patterns such as nanocraters. Fourier images can reflect repeated patterns as narrow peaks, the co-ordinates of which describe the periodicity and direction of the structures. A typical 2–D fast Fourier transform spectra is reported in Paper II, the high-intensity domain spacing rings seen in the reciprocal space indicate that the films have a well-defined short-range order and a fairly narrow distribution of the distance between nanocraters. For a long-range hexagonal ordering, six high-intensity spots would be visible instead of the rings.[73-74] The reciprocal distance of the observed rings from the center of the FFT image can also be used to estimate the pattern periodicity.

5.2.2 Scanning Electron Microscopy (SEM)

As a surface morphology characterization technology, SEM was commercially introduced in the 1960s.[75] In SEM, a beam of electrons emitted from an electron source is focused into a fine probe which impinges on the surface of the target specimen under vacuum conditions.

The electron–specimen interactions result in a number of distinct emission signals, from which images can be derived.[76] A schematic diagram of the working principle of a SEM is shown in Fig. 12.[77]
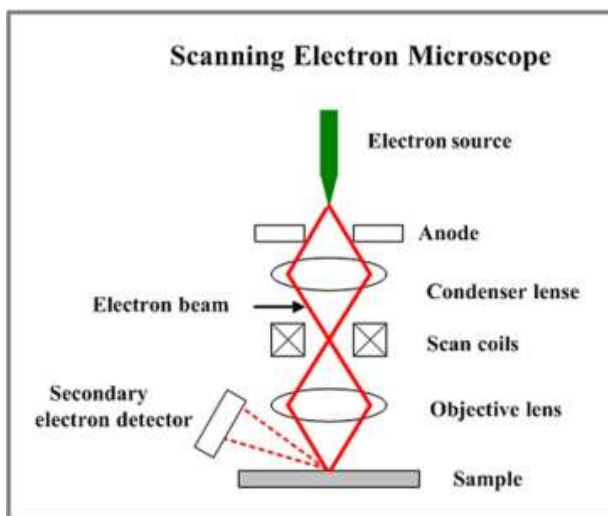
Figure 12. A schematic diagram of the work principle of a SEM.[77]

As shown in Fig. 12, electrons in the electron gun are emitted from and accelerated by the anode. The use of electrons instead of light to form images enables a huge improvement in resolution of SEM in the range of 1 to 20 nm. The electron beam is condensed by the condenser lenses. The electron beam is deflected by the scan coils back and forth and finally focused by the objective lens to a very fine spot (1–5 nm), and scans the sample surface in a raster pattern. Primary electrons interact with the atoms of the sample surface, causing emissions of the secondary electrons, which can be detected and converted to be a photon of light and displayed as a two–dimensional intensity distribution, viewed as an image. A large number of secondary electrons are displayed as bright spots, while darker spots are generated by fewer secondary electrons. Small projections on the sample surface appear bright due to the larger area of shorter path length for the escape of secondary electrons than for flat areas. This is the reason behind the three–dimensional appearance in the SEM image.[78] In addition to imaging, elemental analysis can be also performed by detection and measurement of X–rays, which is referred to as Energy Dispersive X–ray Spectroscopy (EDS).

In this thesis, SEM images were captured by a LEO Gemini 1530 (Oberkochen, Germany) instrument with a Thermo Scientific Ultra Dry Silicon Drift Detector (Madison, Wisconsin,

USA). The acceleration voltage was 2.7 kV and the magnification of the image corresponds to a Polaroid 545 print with the image size of 8.9 cm × 11.4 cm.

5.3 Surface composition and crystallinity

5.3.1 X–ray Photoelectron Spectroscopy (XPS)

XPS, also called Electron Spectroscopy for Chemical Analysis (ESCA), is a powerful surface analysis technique which is able to provide composition and chemical state information of a sample surface with an elemental detection limit in the vicinity of 0.5 atomic percent. An XPS working principle and the corresponding data output spectra for a pure copper surface is shown in Fig. 13.[79]
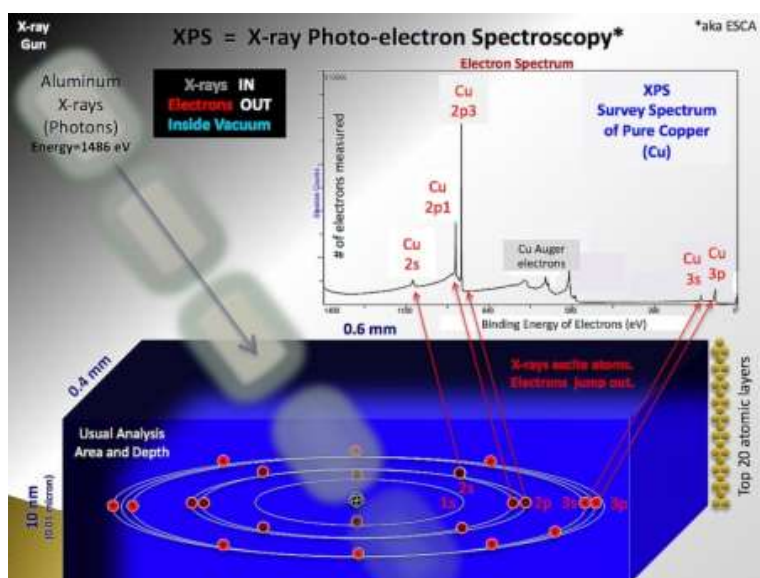
Figure 13. A schematic diagram of the working principle of an XPS.[79]

The Cu is irradiated by x–rays generated by Al Kα (1486.6 eV) excitation sources under ultra–high vacuum conditions. The x–rays penetrate into the sample and liberate electrons from the atoms of the Cu surface with an analysis depth of 5–10 nm. The kinetic energy of the liberated electrons can be calculated according to the equation

$$BE = hv - KE - \phi_s \quad (9)$$

Here BE is the binding energy of the electrons in the atom, hv is the energy of the X–rays, KE is the kinetic energy of the electrons and ϕ_s is the spectrometer work function.

24

An XPS spectrum is usually plotted as the number of electrons versus electron binding energy. Because the binding energies of the electron orbitals in atoms are known, the positions of the peaks in the spectrum allow one to identify the atomic composition of the sample surface and the relative areas of the photoelectron peaks provides quantitative information about different compositions. A survey spectrum including the energy range from 0 eV to 1100 eV, is usually used to determine the elemental composition of the sample surface. A high resolution spectrum usually covers a narrower energy range from 10 to 30 eV, which can be used to determine the surface composition and the chemical environments of a certain element precisely. XPS is widely used for analyzing organic and inorganic systems, including thin films and powders.

5.3.2 Grazing Incidence X–Ray Diffraction (GI–XRD)

XRD is a non–destructive method, which is indispensable for investigation and characterization of materials, including metals, thin–films, ceramics, powders and so on. The principle of XRD is based on the interaction of the incoming x–ray beam with the crystallographic planes in the sample, defined by the Bragg's equation[80], where n is an integer, λ is the X–ray wavelength, d is the inter–planar spacing in the crystal lattice and θ is the angle between the sample surface and the incident beam. An illustration of how a XRD works is shown in Fig. 14.[81]

$$n\lambda = 2d \sin \theta \quad (10)$$

Typically, the x–ray tube is stationary, the sample moves by the angle θ and the detector simultaneously moves by 2θ. As the sample and detector rotate, X–rays diffract at specific angles. The diffractogram consists of a plot of reflected intensities versus the detector angle 2θ. The peak positions, shapes and relative intensities can be directly correlated to crystallographic spacing, phase, and crystallite size. XRD is a fundamental technique, which is complementary to other techniques, such as SEM. Nanoparticle shape or morphology cannot be assessed by XRD, but XRD can identify the crystallinity (amorphous, single crystal or multi–phase) whereas SEM cannot. X–ray diffraction measurements of thin films generally produce a weak signal from the film but an intense signal from the underlying substrate. Thus, a fixed grazing angle of incidence, popularly known as GI–XRD was performed in this thesis to avoid an intense signal from the substrate and get a stronger signal from the film itself. The fixed angle is generally chosen to be slightly above the critical angle for total reflection of the film material.
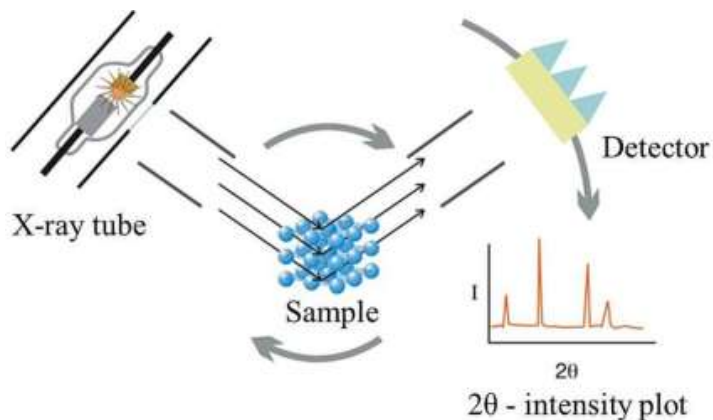
Figure 14. A schematic illustration of the working principle of XRD.[81]

GI–XRD measurements in this thesis were performed with a Bruker AXS D8 Discover instrument (Karlsruhe, Germany). A grazing incidence angle of 0.31° was used for all the measurements. The data was collected between 24 and 40° 2θ using a step size of 0.04° 2θ. The JCPDS (Joint Committee on Powder Diffraction Standards) card numbers 00–021–1272, 01–086–0148 and 01–075–0576 were used to identify the pure anatase TiO_2, rutile TiO_2 and ZnO phases, while $Zn_2Ti_3O_8$, $ZnTiO_3$ and Zn_2TiO_4 were assigned to the 01–087–1781, 01–086–0155 and 01–085–547 JCPDS cards, respectively.

6. RESULTS AND DISCUSSION

6.1 Development of the fabrication of NP-TiO$_2$ thin films

In order to develop the current fabrication system of NP-TiO$_2$ thin films, it deserves to study the background experimentally to get familiar with how all the parameters affect the synthesis. In this section, the surface energy of substrates used in this thesis, the influence of parameters in the EISA process as well as the fabrication techniques is discussed.

6.1.1 Surface energy

The surface energies of the substrates studied in this thesis are summarized in Table 1. Generally, the Zonyl FSE functionalized flat/perforated TiO$_2$ films have much smaller surface energies compared to the other films. Si-wafer and TiO$_2$ reference show similar surface energy and polarity. By introducing a Zonyl monolayer, surface energy and polarity of the TiO$_2$ surface is reduced significantly, which subsequently decrease the wettability of the surface towards both polar and nonpolar liquids. The phosphate head group can chemically bind with TiO$_2$ but only physically adhere to the silicon surface and can therefore be easily removed after rinsing. Thus, no change in surface energy of Si-wafer is observed after Zonyl FSE functionalization.

Table 1. Surface energies of the studied systems.

Surface	Dispersive component mN/m	Polar component mN/m	Total/ mN/m
Si wafer	31	34	65
Si wafer + Zonyl	30	36	66
TiO$_2$ reference	36	30	66
TiO$_2$ reference + Zonyl	12.8	1	14
NP–TiO$_2$	35	33	68
NP–TiO$_2$ + Zonyl	12	2	14

6.1.2 Influence of the molar ratio (*m*) of the metal precursor and the EO group
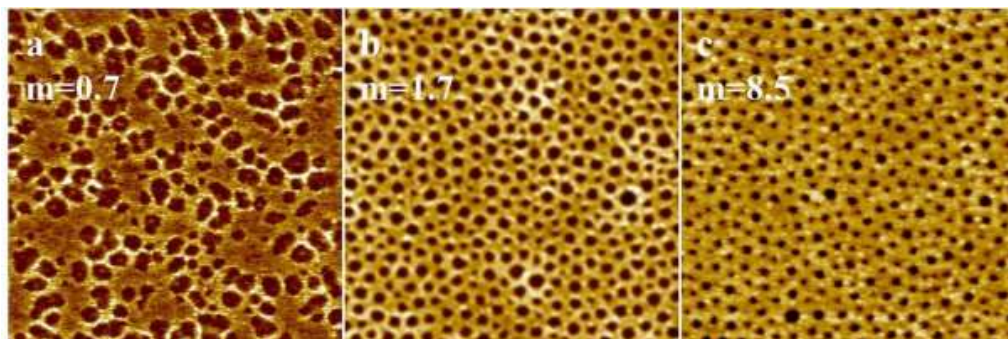
Figure 15. AFM images (1*1 μm) of metal oxide thin films with different m values: a)
m=0.7, b) m=1.7 and c) m=8.5.

For a typical dipping sol, the *m* value (molar ratio between the metal precursor and the ethylene oxide (EO) group in the solution) is 1.7 which resulted in a perforated structure shown in Fig. 15 b, which is taken as the reference nanoperforated TiO_2 thin film in this thesis. The extracted nanocrater size and wall thickness are about 30 nm and 25 nm, respectively. With a small *m* value of 0.7, there were not enough $TiCl_4$ precursors to coordinate with the EO group, leading to random ring structures on the surface instead of well–ordered perforations, shown in Fig. 15 a. Increasing the *m* value to 8.5, the area covered by the craters decreased from 34% to 15% and the height of the film increased from 4.4 nm to 11.2 nm. This result agrees with the conclusion and explanation previously reported.[31]

6.1.3 Influence of the thermal treatment

As shown in Fig. 16 a, a film dried at ambient temperature resulted in a perforated structure with craters having a larger height (11.6 nm) and smaller diameter (20 nm), because here only volatile solvents have evaporated. For the films calcined at 500 °C for 10 minutes (Fig. 16 b), the height is smaller (4.4 nm) and the crater diameter is larger (~30 nm), due to the decomposition of PB–b–PEO at around 200 °C and complete formation of the perforations and crystallinity of the TiO_2 network at 500 °C.[36]
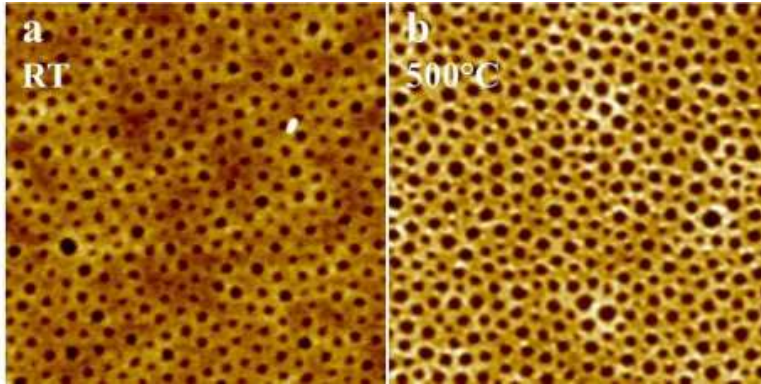
Figure 16. AFM images (1 μm * 1 μm) of NP–TiO$_2$ thin films fabricated at a) RT and b) 500°C.

6.1.4 Comparison of the fabrication techniques and modification of sols
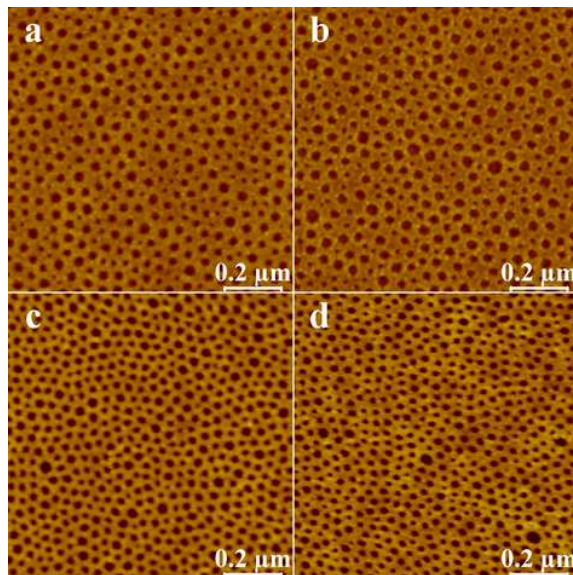
Figure 17. AFM images of dip–coated structures being fabricated using a) an unmodified precursor solution, b) an ink with 5 vol–% BE, c) an ink with 20 vol–% BE and d) a drop–cast ink with 20 vol–% BE.

In the dip-coating process, the deposited area of the nanoperforated oxide thin films is determined by the size of the substrate on which the film is deposited. Inkjet printing, instead, provides the advantage of depositing the ink onto target areas, thus enabling the fabrication of

29

microscale arrays and other patterned structures. However, the final dipping sol is not directly suitable for inkjet printing, due to its low surface tension (23.6 mN/m at 20 °C), low viscosity (0.91 mPas at 20 °C) and especially its low boiling point (74 °C). To improve the jettability, 2–butoxy ethanol (BE) was added as a carrier solvent to the precursor solution. The characteristics of BE are as follows: surface tension: 27.4 mN/m at 20 °C, viscosity: 2.9 mPas at 20 °C and boiling point: 171 °C. It was experimentally determined that up to 20 vol–% of BE can be added to the 70:30 vol–% EtOH/THF solution without altering the solution transparency and stability. The characteristics of the new ink were as follows: density: 0.83 g/ml (at 20 °C), surface tension: 24.7 mN/m, viscosity: 4.10 mPa s (at 20 °C). This yielded a Z–value (the inverse Ohnesorge number) of 5.3, predicting good printability.

Fig. 17 a, b and c show AFM topographs of dip–coated TiO_2 films on a silicon wafer prepared from different solutions. Nanoperforated TiO_2 films with typical perforation morphology were observed for all the samples and the addition of BE did not have any significant effect on the spherical shape (roundness) of the perforations. However, a more close–packed perforation structure was observed when 20 vol–% BE was added. Similar results have been reported by Kuemmel et al., who indicated that the solubility of PB–b–PEO can be improved by using solvents with low polarity (log P_{ow} for BE is 0.83 and for EtOH it is –0.31), as smaller micelles with higher curvatures can be more effectively accommodated by a solvation system with higher dissolution capacity.[11]

Drop-casting was tested as a dispensing method for a precursor solution with 20 vol-% of BE to examine if hydrodynamic conditions (spreading and drying of solvents) more similar to the ones used in inkjet printing would affect the nanostructure of the resulting TiO_2 films. Fig. 17 d shows that a nanoperforated structure was obtained also by drop–casting (i.e., by placing a 0.1 µL droplet of solution on the substrate by a microsyringe). However, compared to the dip–coated film with 20 vol–% of BE (Fig. 17 c), the perforations were smaller and deeper, leading to higher material volume (MV) values (Table 2). A thicker and a more tightly packed film morphology compared to the dip–coated film may result from a limited spreading of the solution due to contact line pinning, which leads to a higher amount of material per area.

Table 2. Morphological parameters obtained from AFM image analysis of NP–TiO$_2$ films prepared by dip–coating, drop–casting and inkjet printing at ambient temperature.

DS/ µm	D[a]/ nm	H[b]/ nm	NND[c]/ nm	RD[d]	MV[e] ×10^6 /nm^3	K[f]/ ×10^{-6} /ml/mm^2
Dip–20%[g]	25.3±5.3	3.1±0.8	38.6±3.4	0.75±0.12	2.34	5.58
Drop[h]	22.7±5.5	4.1±0.7	35.2±3.3	0.65±0.12	3.46	6.18
5		54.5±24.4			1215	404
10	38.5±13.1	9.5±1.6	55.1±6.9	0.75±0.15	7.10	102
20	46.9±18.5	8.1±1.7	57.9±7.6	0.71±0.17	5.15	26.0
30	31.4±14.6	6.1±1.6	42.5±7.1	0.59±0.18	6.10	11.6
40	45.6±23.8	5.2±1.9	55.3±9.9	0.51±0.18	3.67	6.76
50	40.2±13.2	2.6±0.8	48.0±6.5	0.66±0.17	1.79	4.41

[a]Measured mean perforation diameter (D), [b]Mean perforation height measured from the histograms (H), [c]Nearest Neighbor Distance (NND), [d]Roundness (RD), [e]Material Volume (MV), [f]Printed volume/Area (K, the nominal drop volume was 10 pL), [g]Dip–coating with 20 vol–% BE and [h]Drop–casting with 0.1 µL ink.

6.2 Fabrication of nanoperforated TiO$_2$ films by inkjet printing

In Paper I, inkjet printing was successfully used as a cost–efficient means to produce NP–TiO$_2$ thin films at both ambient temperature and 60 °C. As shown in Fig. 18, the darker contrast in the optical micrographs is related to thicker parts of the films and these regions generally showed more poorly defined nanoperforation morphology. On the other hand, AFM images captured from thinner regions had clearly defined nanoperforation morphologies and good reproducibility. The AFM images discussed in this section are all captured from the thin parts of the printed films.

The effect of evaporation time on print quality and TiO$_2$ morphology was studied by heating the substrate during printing (using multiple nozzles). The heating plate temperature was set to 60 °C. The microscope image in Fig. 18 show that areas being printed at 60 °C (DS 20 µm) appear to be more heterogeneous compared to the ones being printed at ambient temperature. However, coffee–ring[82] and bulging effects[83–84] at the edge of the areas had decreased and the areas had approximately the same diameter. With larger DS values (30–50 µm), substrate heating generated a better distribution of the ink on the surface and the areas became less visible.
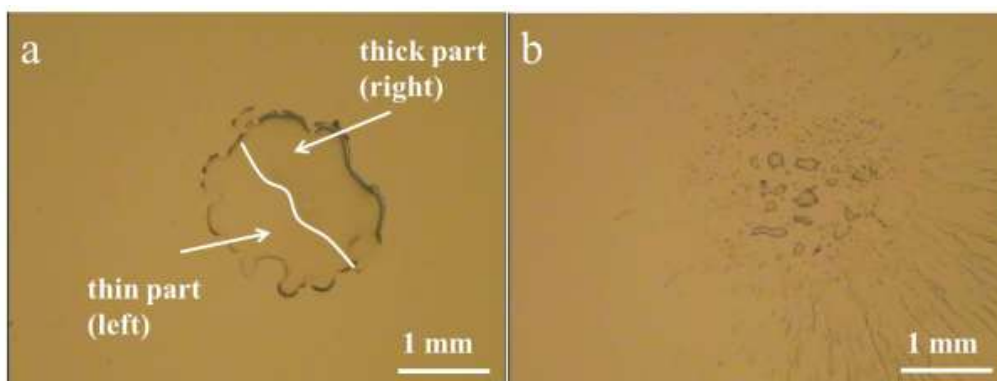
Figure 18. Microscope images of TiO₂ structures prepared by inkjet printing with DS 20 μm at a) ambient temperature and b) 60 °C.
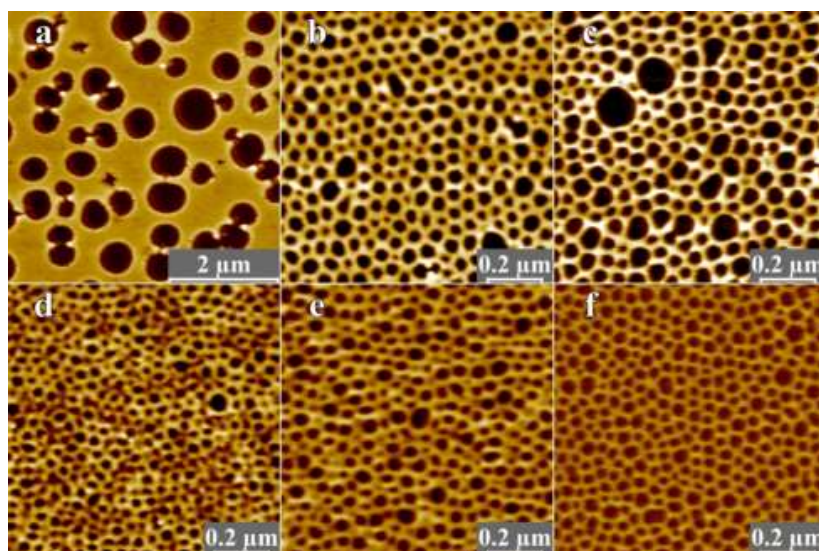
Figure 19. AFM images of NP–TiO₂ films prepared by inkjet printing with DS a) 5 μm, b) 10 μm, c) 20 μm, d) 30 μm, e) 40 μm and f) 50 μm at ambient temperature.

Fig. 19 shows AFM topographs of NP–TiO₂ films prepared by inkjet printing at ambient temperature. The structures in Fig. 19 a and d were also analysed by SEM (Fig. 20). Table 2 lists the morphological parameters obtained from the respective AFM images. Excluding the TiO₂ film printed with DS 5 μm, all the samples show quite a uniform nanoperforated structure. The average height (H) of the nanoperforations increased with increasing amount of

ink deposited per area (K). When comparing the H values of the samples with approximately similar K values, it is evident that the deposition method did not have a significant effect on the perforation height.
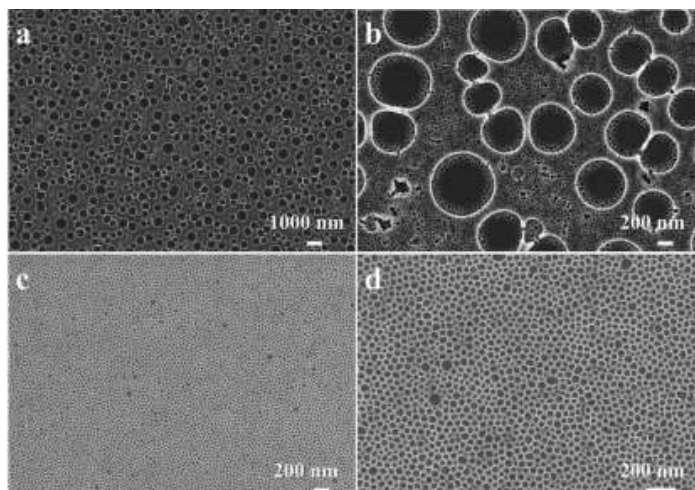
Figure 20. SEM images of TiO$_2$ structures prepared by inkjet printing with different DS values at ambient temperature. a) and b) show the DS 5 µm film at magnifications of 5k and 25k, respectively; c) and d) show the DS 30 µm film at magnifications of 25k and 50k, respectively.

When excessive precursor amounts were printed with DS 5 µm, the TiO$_2$ film consisting of hierarchical surface structure with micro–sized and nano–sized perforations was confirmed by both AFM (Fig. 19 a) and SEM (Fig. 20 a and b). The formation of micrometer-sized perforations is related to the spinodal decomposition mechanism which has earlier been shown for dip-coated films.[38] A similar structure can be achieved by phase separation between the solvent and block copolymer/TiO$_2$ species at the point of gelation in this study.
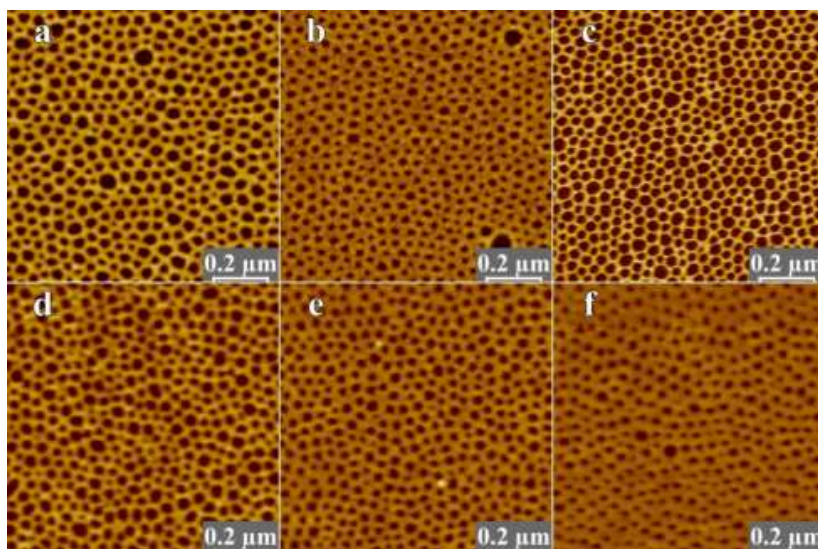
Figure 21. AFM images of NP–TiO$_2$ films prepared by inkjet printing with DS a) 5 µm, b) 10 µm, c) 20 µm, d) 30 µm, e) 40 µm and f) 50 µm at 60 °C.

Fig. 21 shows AFM topographs of samples printed using substrate heating, which show the typical perforation morphology. The height values of the films are fluctuating close to the values observed for the dip–coated and drop–cast films. Compared to ambient temperature, inkjet printing at 60 °C provided a narrower height distribution of about 5 nm. These results further indicate that the printing conditions which involve less bulging and faster drying are more optimal for formation of nanoperforated TiO$_2$ films. However, to improve the macroscopic homogeneity, a careful optimization of the jetting frequency, temperature and drop spacing has to be done.

6.3 Synthesis of nanoperforated zinc titanate thin films

In Paper II, the possibility of expanding the EISA concept of producing nanopatterned thin films to include ternary metal oxides was demonstrated. As an example shown in Fig. 22, it was chosen to prepare mixed zinc–titanium oxide films with various Zn/Ti molar ratios.
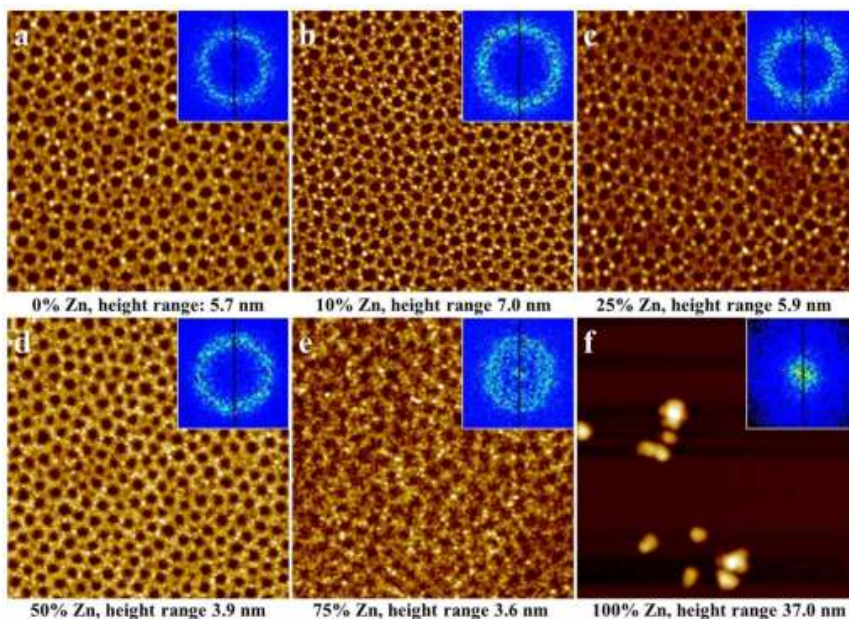
Figure 22. AFM images (1 μm * 1 μm) of metal oxide films with different molar fractions of Zn. In the insets the corresponding FFT images in the range of q=0–30 μm^{-1} are shown.

The sample with 0% Zn corresponds to the well–studied reference nanoperforated TiO_2 film with no added $ZnCl_2$ (Fig. 22 a). The ordering of the crater structures can be evaluated from 2–D fast Fourier transform (2–D FFT) spectra calculated from the AFM height images as shown in the insets. Similar 2–D FFT analyses for self–assembled block copolymers have been performed previously by other groups.[73-74]

As seen in Fig. 22, replacing equimolar amounts of $TiCl_4$ with $ZnCl_2$ in the dipping solution does not seem to alter the nanocrater structure noticeably even up to 50 mol% of Zn. With higher amounts of Zn the film structure becomes increasingly disordered as seen in the AFM image of sample 75% Zn, and also evidenced by the 2–D FFT pattern with increasing scattering. In addition, the film for the sample 75% Zn was clearly thinner (~0.6 nm) as compared with samples with lower Zn content, which indicates that the nanocraters could also be filled with some Zn/Ti oxide. This is also corroborated by the fact that the nanocrater coverage is smaller for this sample (~12% compared to 18% for the other samples). Finally, an attempt to make a pure ZnO nanopatterned film was carried out by completely substituting the $TiCl_4$ with $ZnCl_2$ (sample 100% Zn). However, as seen in the AFM image in Fig. 22 f, no

crater structure was obtained. Instead, a coarse particulate structure with an estimated grain size of roughly 50 nm was formed.

GI–XRD measurements were utilized to obtain more information about the chemical nature (i.e. the crystal phase) of the metal oxide films. As seen in Fig. 23, the pure TiO_2 film (0% Zn) calcined at 700 °C shows a clear reflection centered at around 25.5° 2θ and three overlapping reflections at 37.2°, 38.0° and 38.6° 2θ, which all originate from the anatase form of TiO_2. The relatively wide reflections also indicate that the sample is nanocrystalline.
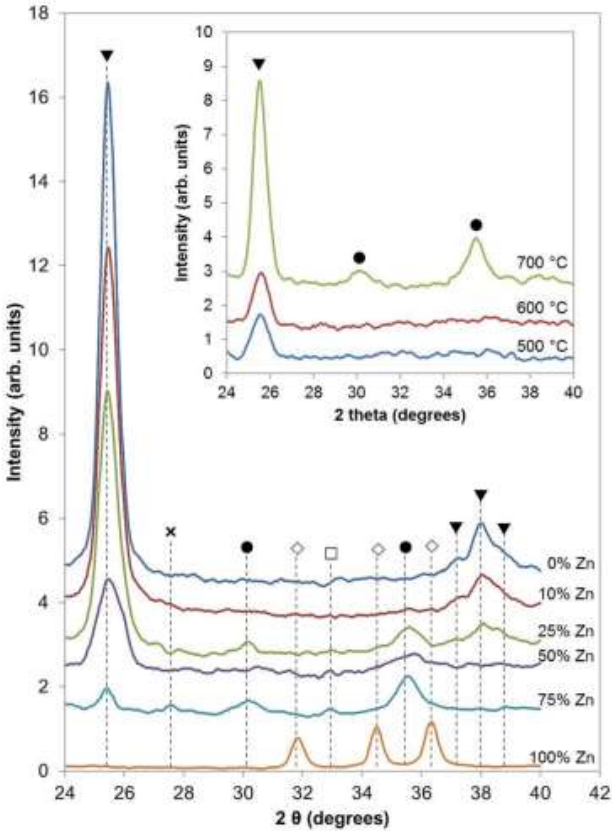
Figure 23. GI–XRD patterns of zinc titanate films with different Zn content calcined at 700 °C. Reflections denoted by ▼ belong to the anatase TiO_2 phase, while ✕ = rutile TiO_2, ● = $Zn_2Ti_3O_8$, ◇ = ZnO, and □ = $ZnTiO_3$, respectively. The inset shows XRD patterns of zinc titanate films (50% Zn) calcined at different temperatures.

As a consequence of increasing the Zn/Ti ratio, the intensity of the anatase diffraction peaks decreased gradually from sample 0% Zn to 75% Zn, which is to be expected when the pure anatase phase is consumed at the expense of the formation of new zinc titanate phases.[85] The main zinc titanate phase observed in all the mixed oxide samples belongs to the cubic defect spinel structure of $Zn_2Ti_3O_8$ as evidenced by the appearance of the two diffraction peaks at around 30.1° and 35.5° 2θ in Fig. 23. The inset also implies that a calcination temperature of 700 °C is required to obtain the $Zn_2Ti_3O_8$ phase for these thin films. At high zinc contents in the films (between 50 and 75%), a diffraction peak at ~32.8° indicates small amounts of $ZnTiO_3$. Finally, the 100% Zn sample consists only of the pure wurtzite ZnO phase, which usually appears for thicker films at temperatures above 200 °C.[86]

The observations above can generally be explained by the partial charge model concept introduced by Jolivet and coworkers.[87] The ease of obtaining a well–structured titania/zinc titanate nanostructure at low $ZnCl_2$ ratios is mainly dictated by the presence of the $TiCl_4$ compound. Solvated Ti^{4+} ions are easily hydrolyzed in aqueous solutions which results in a low pH value (as in the present case, the pH is about 0). The resulting aqua–hydroxido complex $[Ti(OH)_2(OH_2)_4]^{2+}$ can easily undergo sol–gel condensation reactions, while at the same time interacting strongly with the hydrophilic PEO corona of the PB–b–PEO block copolymer micelles. Already at the solvent evaporation stage in the dip–coating process, a cross–linked amorphous TiO_2 network is formed surrounding the block copolymer template, which leads to a nanoperforated hybrid thin film. The highly acidic media due to Ti(IV) hydrolysis and the presence of ethanol preclude the formation of EO-Ti complexes except in practically dried gels, which has been thoroughly studied in the work by Soler-Illia et al.[88] On the other hand, solvated $ZnCl_2$ is more stable in its pure aqua form $[Zn(OH_2)_6]^{2+}$, which does not affect the pH of the solution much and does not normally undergo condensation reactions. However, in the presence of the $[Ti(OH)_2(OH_2)_4]^{2+}$ complex, solvated Zn^{2+} can also partake in the condensation reaction, as the nucleophilic hydroxido ligands in the titanium aqua–hydroxido complex can readily replace the aqua ligands in the $[Zn(OH_2)_6]^{2+}$ complex. At an excess of the ZnO precursor (e.g., at 75% Zn), the deficient amount of the TiO_2 precursor cannot provide enough nucleophilic hydroxide ligands to fully condense both metal compounds, leading to a less cross–linked metal oxide/hydroxide structure.

In addition to the chemical composition of the as–synthesized thin films, also the nanostructure appears to have a large influence on the crystal phase of the final calcined

materials. The preferred crystalline phases obtained for the mixed Zn–Ti oxide samples are anatase TiO_2 and the spinel type $Zn_2Ti_3O_8$, which both have common three–dimensional frameworks of TiO_6 octahedra that are connected over four common edges.[89–90] On the other hand, in the rutile form of TiO_2 and for $ZnTiO_3$, the connection of the TiO_6 octahedra leads to chains and/or layers. It would be expected that the less–constrained anatase–type molecular construction would be better compatible with the extremely thin nanoperforated film structures obtained for the zinc titanate samples up to 50% Zn.[90]

The only sample where crystalline ZnO could be detected is for the pure ZnO sample (100% Zn), where larger crystallites could be observed rather than a nanoperforated thin film structure. Since ZnO shows a highly anisotropic growth rate along the c axis, which prefer–ably leads to one–dimensional nanostructures[91], the absence of a crystalline ZnO phase in the well–ordered zinc titanate films is not unexpected.

6.4 Wetting studies of hydrophilic–hydrophobic $TiO_2@SiO_2$ nanopatterns

The perforated $NP–TiO_2$ thin film on the SiO_2 substrate represents a two-component composite surface, where the SiO_2 substrate is accessible through the craters in the $NP–TiO_2$ film (Fig. 9). The craters are evenly distributed and the diameter of the craters can be tuned between 10 to 50 nm, depending on the molecular weight of the templating surfactant. The open pore structure and high homogeneity of the crater morphology as well as the tunability of crater sizes make the $NP–TiO_2$ thin films (referred to as $TiO_2@SiO_2$ composite in this paper) ideal for detailed wetting studies. In Paper III, the films were initially functionalized with a fluoroalkylsilane (FAS), resulting in hydrophobic surfaces on both titania and silica. As shown in Fig. 24 a, all FAS–functionalized surfaces are hydrophobic with static water contact angles ~107° before UV treatment. These contact angle values are close to values observed for fully fluorinated surfaces, indicating a full coverage of the fluoroalkylsilane layer on the surface.[92] The close agreement between the contact angles suggests that the surface roughness of the TiO_2/SiO_2 composite is small and thereby has a negligible effect on wetting.

The surfaces were then exposed to UV light and the FAS layer was degraded only on the titania patches, due to the different photocatalytic properties of titania and silica.[93–94] A schematic description of the photocatalytic decomposition on the $TiO_2@SiO_2$ surfaces was presented in Fig. 9 b. The water contact angle on a FAS-functionalized SiO_2 reference remained unchanged after a UV treatment of 120 minutes, indicating that the FAS layer on

SiO$_2$ was not modified by the UV exposure, see Fig. 24 a. On the other hand, the water contact angle on a FAS functionalized TiO$_2$ reference decreased dramatically to ~5° even after a short UV treatment of 5 minutes. As expected, the water contact angle decreased gradually on the FAS–coated TiO$_2$@SiO$_2$ sample as a function of UV treatment time within 60 minutes, after which the decrease became less obvious.

By using the Cassie[43] and Israelachvili[45] wetting models for heterogeneous surfaces, the area fraction covered with FAS (f_{FAS}) can be calculated from water contact angle measurements from equations (11) and (12), respectively, where θ_{COMP} is the water contact angle on the composite surface, θ_{TiO_2} is the contact angle on the UV treated TiO$_2$ reference surface and θ_{FAS} is the contact angle on the hydrophobic FAS layer. The results were compared to the area fractions derived from XPS measurements.
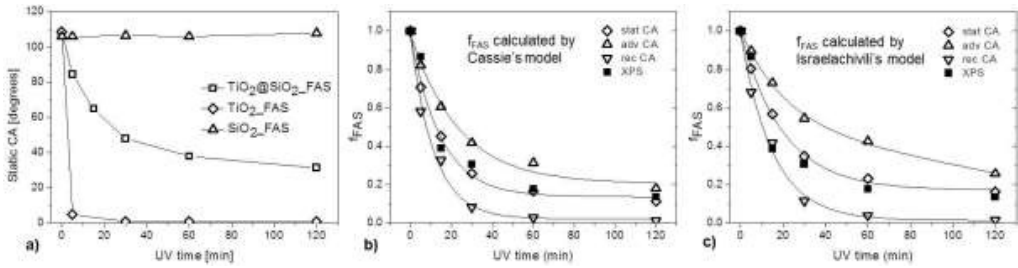
Figure 24. a) CA as a function of UV treatment time on different surfaces, b) f_{FAS} **values calculated by Cassie's model and c)** f_{FAS} **values calculated by Israelachivili's model.**

$$f_{FAS} = \frac{\cos\theta_{COMP} - \cos\theta_{TiO_2}}{\cos\theta_{FAS} - \cos\theta_{TiO_2}} \ (11) \qquad \text{and} \qquad f_{FAS} = \frac{(1-\cos\theta_{COMP})^2 - (1-\cos\theta_{TiO_2})^2}{(1-\cos\theta_{FAS})^2 - (1-\cos\theta_{TiO_2})^2} \ (12)$$

As shown in Fig. 24 b and c, the f_{FAS} values determined from static water contact angles fit best with XPS data, while the advancing and receding contact angles overestimated and underestimated the f_{FAS}–values, respectively. The good fit of f_{FAS} values derived from the static contact angle to the XPS results suggests that these models are valid to describe the wetting phenomenon on the TiO$_2$@SiO$_2$ surfaces, where the length scale of the heterogeneities is very small compared to the size of the droplet. Since the Israelachvili model was derived for chemical heterogeneities of atomic or molecular dimensions, the conclusion

that the Cassie's model gave a slightly better fit to the XPS data than the Israelachivili's model is quite logical.

Fisher et al.[10] has confirmed that these systems are composed of nanometer–sized domains and the proportion of domains crossed by the three-phase contact line is close to the corresponding area fraction, and the related water contact angle measurements can be described satisfactorily by the Cassie model. Järn et al.[13] revealed that there is a shift from Cassie–Baxter to Cassie–Wenzel–type wetting when a droplet volume increased from 2 µL to 6.5 µL. The larger contact angle hysteresis suggests a possible existence of an intermediate state between the Cassie–Baxter and Cassie–Wenzel modes. For these ordered craters, the r value (the ratio of the actual and projected surface areas of the sample) was calculated from crater radius, height and wall thickness obtained from AFM, SEM and ellipsometry measurements. Simply by tuning the synthesis and modification process, the nano–perforated surface can provide a versatile system for the research of wetting phenomena, in both the nano–micro and the macro scale.

6.5 Fabrication of nanoperforated polymeric films by inkjet printing

In Paper IV, various functional materials were inkjet-printed on the nanoperforated TiO_2 substrates that acted as nano–templates for producing thin (1–5 nm) polymer films with similar topography. In principle, it is possible to use any type of ink as long as the material solidifies after drying, so the method is not only limited to polymers. In this work dispersions of conductive and bio–functionalized polymers were used as model inks as they show interesting electronic and optical properties. The conductivity and reactivity of the polymers was expected to increase due to their intimate contact with the nanoperforated TiO_2 structure.[95] Recently printing of a biotinylated polythiophene derivative (PBTL) has been reported. This material is of great interest in the field of biosensors, as the biotin groups can act as an anchoring layer for streptavidin and other avidins.[96–97] The other polymer that was investigated here, dinonylnaphthalene sulfonic acid–doped polyaniline (PANI–DNNSA), is widely used in electrochemistry for its redox/protonation properties as well as its potential in gas sensing.[98–99]

Fig. 25 a and d show AFM topographical images (1 µm × 1 µm) captured at the non–printed section and the section printed with a PBTL ink on NP–TiO₂, respectively. Both images show well–defined nanoperforated topography as expected. The differences between the non–

printed and printed images are more obvious from the corresponding height histograms (Fig. 25 b and e) and phase images (Fig. 25 c and f).
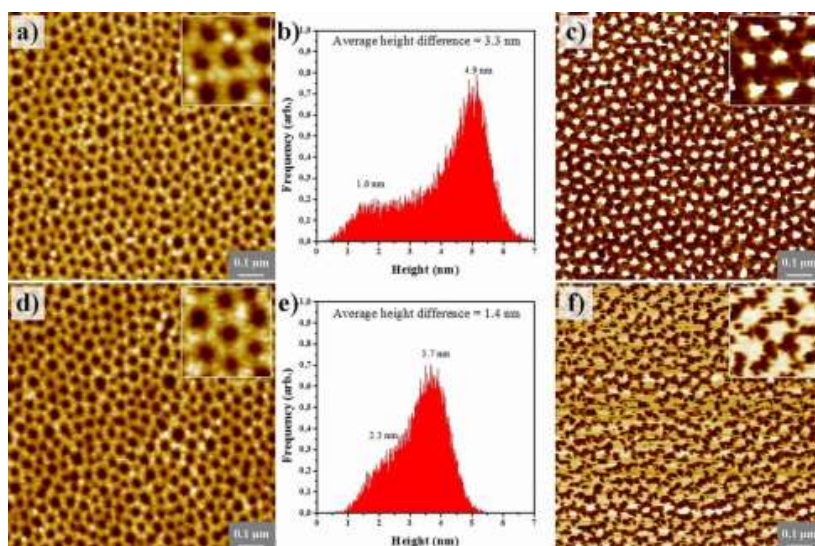
Figure 25. a) AFM topographic image and b) the corresponding histogram, and c) phase image for the NP–TiO$_2$ substrate; and d) AFM topographic image and e) the corresponding histogram, and f) phase image for the NP–TiO$_2$ substrate with inkjet–printed PBTL. The size of the inset images is 150 nm × 150 nm.

The height histogram of the image captured at non–printed section of the NP–TiO$_2$ substrate shows two clearly separated peaks with a peak–to–peak distance of 3.3 nm (Fig. 25 b). This can be interpreted to be the average height of the nanoperforated TiO$_2$ network overlayer on SiO$_2$. In addition, Fig. 25 c shows a difference in phase contrast between the bottom of the perforations (SiO$_2$) and the network overlayer (TiO$_2$). TiO$_2$ and SiO$_2$ are both relatively hard materials (compared to the silicon tip) and visco–elastic interactions between the tip and the surface are expected to be negligible. Thus, the phase contrast difference most probably arises from the adhesive interactions, where the silicon tip to SiO$_2$ shows a higher adhesion (brighter contrast, average phase angle 146°) compared to the TiO$_2$ network (average phase angle 88°).

Contrary to the image captured at the non–printed section, the height histogram of the image captured at the PBTL–printed section of NP–TiO$_2$ substrate does not show a clear peak separation but only a shoulder to the left of the main peak (Fig. 25 e). The shoulder-to-peak distance is about 1.4 nm. The decrease in height difference between the perforated area and the ridge area indicates that a thicker polymer layer is formed inside the perforations (i.e. on

the exposed SiO$_2$ surface) compared to on top of the TiO$_2$ ridges. In addition, the phase difference between the perforations and the overlayer structure is less obvious (Fig. 25 f). Although the phase image is not totally homogenous and shows two contrast regions, these regions are not directly coupled to the topographical features as was the case for the non–printed section. The brighter contrast (average phase angle 130 degrees) dominates the phase image and follows both TiO$_2$ and SiO$_2$ regions of the topograph. On the other hand, the dark contrast (average phase angle 99 degrees) solely follows the TiO$_2$ overlayer. The average phase angle values of the two regions do not match the values of the non–printed section. This is relevant considering that the same tip and measuring parameters were used to capture the images. The results above indicate that the PBTL polymer film fully covers the nanoperforated structure and is distributed evenly on both the TiO$_2$ and SiO$_2$ areas. However, the heterogeneous phase image suggests that the polymer is interacting differently with the tip depending on its location. This might be due to different thickness of the polymer film at the two different regions as indicated by the difference in the height histograms (Fig. 25 e). Furthermore, the interaction between the tip and the polymer can also be affected by the underlying surface (TiO$_2$ or SiO$_2$). In addition, local variations in orientation or density of the polymer film can contribute to different tip–polymer interactions.[100]
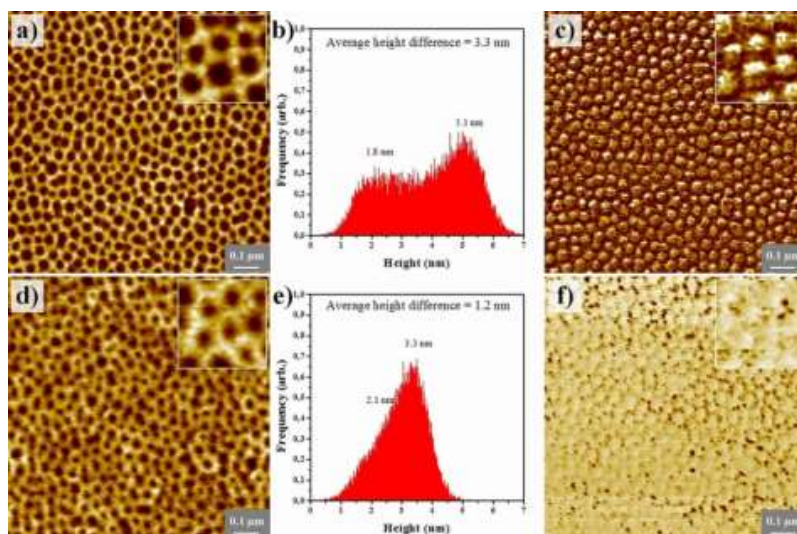

Figure 26. a) AFM topographic image and b) the corresponding histogram, and c) phase image for NP–TiO$_2$ substrate; and d) AFM topographic image and e) the corresponding histogram, and f) phase image for NP–TiO$_2$ with inkjet–printed PANI–DNNSA. The size of the inset images is 150 nm × 150 nm.

PANI–DNNSA was also inkjet printed on NP–TiO$_2$ substrates and the results are quite similar to what was observed for the PBTL film. AFM topographical images show that the typical nanoperforated structure of the NP–TiO$_2$ substrate is retained after inkjet–printing of the PANI–DNNSA film (Fig. 26 a and d). The height histograms show that the peak to peak distance decreased from 3.3 nm (Fig. 26 b) to 1.2 nm (Fig. 26 e) after printing, suggesting a larger accumulation of PANI–DNNSA in the perforations. In addition, a more homogeneous phase contrast and about 30 degrees higher mean phase angle value was observed for the printed polymer sample (Fig. 26 f) compared to the non–printed substrate (Fig. 26 c).

Further evidence of successful deposition of thin PBTL and PANI–DNNSA layers on the NP–TiO$_2$ substrates was obtained from XPS measurements. As shown in Table 3, the elements sulfur and nitrogen were not present on the NP–TiO$_2$ substrates but were both detected after inkjet printing PBTL and PANI–DNNSA, respectively. A clear increase in the relative at–% ratio of elemental carbon also indicates a thicker polymer layer after deposition of PANI–DNNSA compared to PBTL using the same printing settings, which is probably reflected by the higher polymer concentration in the case of the PANI–DNNSA ink solution.

Table 3. Chemical composition and atomic percentage (at%) for the pure NP–TiO$_2$ substrate and those inkjet–printed with PBTL and PANI–DNNSA.

Substrates/films	Elemental composition (at–%)					
	O	Ti	Si	C	S	N
NP–TiO$_2$	47.6	18.7	10.5	22.8	–	–
NP–TiO$_2$+PBTL	44.0	12.0	10.0	29.0	3.0	1.0
NP–TiO$_2$+PANI–DNNSA	2.3	0.6	0.4	95.7	0.5	0.5

7. CONCLUSIONS AND OUTLOOK

In this study, the synthesis conditions of NP–TiO$_2$ thin films were optimized. Firstly, inkjet printing was successfully used as a cost–efficient means to produce NP–TiO$_2$ thin films on the target areas; secondly, ternary metal oxide systems were studied, where well–ordered zinc titanate nanoperforated thin films with different Zn/Ti ratios were produced; thirdly, the NP–TiO$_2$ films were used to study the validity of Cassie and Israelachivili wetting models; finally, polymeric films were prepared by inkjet printing on NP–TiO$_2$ films, resulting in morphologies similar to that of the unprinted substrate.

Future interesting work in this field could include the fabrication of thicker NP–TiO$_2$ films (with height of 500 nm or more) with similar surface morphology. Larger thickness of the film would on one hand provide sufficient material on the surface, and on the other hand, overcome the roughness limitation of some substrates, e.g., ITO, to improve the fabrication of solar cells. The surfaces with high structured morphology and locally controlled surface energy can provide a useful tool to improve the understanding of wetting phenomena. This can conversely lead in many practical new applications in the fields of cell growth.

To improve the efficiency, novel advanced devices such as gas sensors, solar cells and data storage equipment often require both precise and complicated structures at nanometer scale and controlled patterned structures at macro scale. In this study, inkjet printing has been approved to be an effective tool for the fabrication of NP-TiO$_2$ thin films. This method enables deposition of patterned nanoperforated metal oxide thin films which may enable the design of completely new device configurations.

8. REFERENCES

1. Dameron, A. A.; Davidson, S. D. ; Burton, B. B. ; Carcia, P.F.; Mclean, R. S. ; George, S. M. Gas Diffusion Barriers on Polymers Using Multilayers Fabricated by Al_2O_3 and Rapid SiO_2 Atomic Layer Deposition. *J. Phys. Chem. C*. **2008,** 112(12), 4573–4580.

2. Yang, M. Q.; He, J. H.; Hu, X. C.; Yan, C. X.; Cheng, Z. X. CuO Nanostructures As Quartz Crystal Microbalance Sensing Layers for Detection of Trace Hydrogen Cyanide Gas. *Environ. Sci. Technol*. **2011,** 45(14), 6088–6094.

3. Qin, H. C.; Li, W. Y.; Xia, Y. J.; He, T. Photocatalytic Activity of Heterostructures Based on ZnO and N–Doped ZnO. *Appl. Mater. Interfaces.* **2011,** 3(8), 3152–3156.

4. Song, Y. Q.; Liu, H. M.; He, D. H. Effects of Hydrothermal Conditions of ZrO_2 on Catalyst Properties and Catalytic Performances of Ni/ZrO_2 in the Partial Oxidation of Methane. *Energy Fuels*. **2010,** 24, 2817–2824.

5. Nanu, M.; Schoonman, J.; Goossens, A. Nanocomposite Three–Dimensional Solar Cells Obtained by Chemical Spray Deposition. *Nano. Lett*. **2005,** 5(9), 1716–1719.

6. Stewart, M. E.; Motala, M. J.; Yao, J.; Thompson, L. B.; Nuzzo, R. G. Unconventional methods for forming nanopatterns. *Proc. Inst. Mech. Eng. Part N, J. Nanoeng. Nanosyst.* **2007,** 220, 81–138.

7. Guo, L. J. Nanoimprint Lithography: Methods and Material Requirements. *Adv. Mater.* **2007,** 19, 495–513.

8. Brinker, C. J.; Lu, Y.; Sellinger, A.; Fan, H. Evaporation–Induced Self–Assembly: Nanostructures Made Easy. *Adv. Mater.* **1999,** 11(7), 579–585.

9. Grosso, D.; Cagnol, F.; Soler–Illia, G. J. de A. A.; Crepaldi, E. L.; Amenitsch, H.; Brunet–Bruneau, A.; Bourgeois, A.; Sanchez, C. Fundamentals of Mesostructuring Through Evaporation–Induced Self–Assembly. *Adv. Funct. Mater.* **2004,** 14(4), 309–322.

10. Fisher, A.; Kuemmel, M.; Järn, M.; Lindén, M.; Boissière, C.; Nicole, L.; Sanchez, C. ; Grosso, D. Surface Nanopatterning by Organic/Inorganic Self–Assembly and Selective Local Functionalization. *Small.* **2006,** 2(4), 569–574.

11. Kuemmel, M.; Allouche, J.; Nicole, L.; Boissière, C.; Laberty, C.; Amenitsch, H.; Sanchez, C.; Grosso, D. A chemical solution deposition route to nanopatterned inorganic material surfaces. *Chem. Mater.* **2007,** 19, 3717–3725.

12. Faustini, M.; Capobianchi, A.; Varvaro, G.; Grosso, D. Highly controlled dip-coating deposition of fct FePt nanoparticles from layered salt precursor into nanostructured thin films: An easy way to tune magnetic and optical properties. *Chem. Mater.* **2012,** 24, 1072-1079.

13. Järn, M.; Brieler, F. J.; Kuemmel, M.; Grosso, D.; Lindén, M. Wetting of Heterogeneous Nanopatterned Inorganic Surfaces. *Chem. Mater.* **2008,** 20, 1476–1483.

14. Tekin, E.; Smith, P. J.; Schubert, U. S. Inkjet printing as a deposition and patterning tool for polymers and inorganic particles. *Soft. Matter.* **2008,** 4, 703–713.

15. Sawyer, B. F.; Eric, J. W.; Joseph M. J. Ink–Jet Printed Nanoparticle Microelectromechanical Systems. *J. Microelectromech. S.* **2002,** 11, 54–60.

16. Mougenot, M.; Lejeune, M.; Baumard, J. F.; Boissière, C.; Ribot, F.; Grosso, D.; Sanchez, C.; Noguera, R. Ink Jet Printing of Microdot Arrays of Mesostructured Silica. *J. Am. Ceram. Soc.* **2006,** 89(6), 1876-1882.

17. Fousseret, B.; Mougenot, M.; Rossignol, F.; Baumard, J. F.; Soulestin, B.; Boissière, C.; Ribot, F.; Jalabert, D.; Carrion, C.; Sanchez, C.; Lejeune, M. Inkjet-Printing-Engineered Functional Microdot Arrays Made of Mesoporous Hybrid Organosilicas. *Chem. Mater.* **2010,** 22, 3875-3883.

18. Li, Z. X.; Shi, F. B.; Ding, Y.; Zhang, T.; Yan, C. H. Facile Synthesis of Highly Ordered Mesoporous ZnTiO$_3$ with Crystalline Walls by Self-Adjusting Method. *Langmuir.* **2011,** 27, 14589-14593.

19. Brinker, C. J.; Scherer, G. W. Sol-Gel Science, United Kingdom Edition published by Academic Press Limited, **1990,** 2.

20. Holmberg, K.; Jönsson, B.; Kronberg, B.; Lindman, B. Surfactants and polymers in aqueous solution, **2002,** Great Britain.

21. Kepert, D. L. The Early Transition Metals, Academic press, **1972,** London.

22. Wang, B.; Truhlar, D. G. Partial Atomic Charges and Screened Charge Models of theElectrostatic Potential. *J. Chem. Theory Comput.* **2012,** 8, 1989−1998.

23. Soja, G. R.; Watson, D. F. TiO$_2$–Catalyzed Photo degradation of Porphyrins: Mechanistic Studies and Application in Monolayer Photolithography. *Langmuir.* **2009,** 25(9), 5398–5403.

24. Unruh, D. A.; Mauldin C.; Pastine, S. J.; Rolandi, M.; Fréchet, J. M. J. Bifunctional Patterning of Mixed Monolayer Surfaces Using Scanning Probe Lithography for Multiplexed Directed Assembly. *J. AM. CHEM. SOC.* **2010,** 132(20), 6890–6891.

25. Olivier, C.; Vesselin, N. P.; Orlin, D. V. Fabrication of asymmetrically coated colloid particles by microcontact printing techniques. *J. Mater. Chem.* **2003,** 13, 2445–2450.

26. Zhou, C. H.; Pradeep, R. R.; Justin, W.; Li, X. L.; Punit, K. Photo–Pens: A Simple and Versatile Tool for Maskless Photolithography. *Langmuir.* **2010,** 26(22), 17726–17732.

27. Ulman, A. Formation and Structure of Self–Assembled Monolayers. *Chem. Rev.* **1996,** 96, 1533–1554.

28. Love, J. C.; Estroff, L. A.; Kriebel, J. K.; Nuzzo, R. G.; Whitesides, G. M. Self– Assembled Monolayers of Thiolates on Metals as a Form of Nanotechnology. *Chem. Rev.* **2005,** 105, 1103–1169.

29. Jeong, S. J.; Xia, G.; Kim, B. H.; Shin, D. O.; Kwon, S. H.; Kang, S. W.; Kim, S. O. Universal Block Copolymer Lithography for Metals, Semiconductors, Ceramics, and Polymers. *Adv. Mater.* **2008,** 20, 1898–1904.

30. Pernites, R. B.; Felipe, M. J. L.; Foster, E. L. Advincula, R. C. Colloidally Templated Two–Dimensional Conducting Polymer Arrays and SAMs: Binary Composition Patterning and Chemistry. *Appl. Mater. Interfaces.* **2011,** 3, 817–827.

31. Kuemmel, M.; Boissière, C.; Nicole, L.; Sanchez, C.; Laberty–Robert, C.; Grosso, D. Highly ordered metal oxide nanopatterns prepared by template–assisted chemical solution deposition. *J Sol–Gel Sci Technol.* **2008,** 48, 102–112.

32. Hench, L. L.; West, J. K. The Sol–Gel Process. *Chem. Rev.* **1990,** 90, 33–72.

33. Miao, Z.; Xu, D. S.; Ouyang, J. H.; Guo, G. L.; Zhao, X. S.; Tang, Y. Q. Electrochemically Induced Sol–Gel Preparation of Single–Crystalline TiO$_2$ Nanowires. *Nano. Lett.* **2002,** 2(7), 717–720.

34. Soler-Illia, G. J. A. A.; Innocenzi, P. Mesoporous Hybrid Thin Films: The Physics and Chemistry Beneath. *Chem. Eur. J.* **2006,** 12, 4478 – 4494.

35. Fo1rster, S.; Berton, B.; Hentze, H. P.; Kra1mer, E.; Antonietti, M.; Lindner, P. Lyotropic Phase Morphologies of Amphiphilic Block Copolymers. *Macromolecules.* **2001,** 34(13), 4610–4623.

36. Faustini, M. Nanotexturation par auto–assemblage: Une approche alternative au stockage des informations. Doctoral thesis, **2011,** Laboratoire de Chimie de la Matière Condensée de Paris, Université Pierre et Marie Curie (Paris VI).

37. Kuemmel, M.; Smått, J. H.; Boissière, C.; Nicole, L.; Sanchez, C.; Lindén, M.; Grosso, D. Hierarchical inorganic nanopatterning (INP) through direct easy block–copolymer templating. *J. Mater. Chem.* **2009,** 19, 3638–3642.

38. Kajihara, K.; Yao, T. Macroporous Morphology of the Titania Films Prepared by a Sol–Gel Dip–Coating Method from the System Containing Poly(Ethylene Glycol). III. Effect of Chemical Additives. *J. Sol–Gel. Sci. Techn.* **1999,** 16, 257–266.

39. Faustini, M.; Louis, B.; Albouy, P. A.; Kuemmel, M.; Grosso, D. Preparation of Sol–Gel

Films by Dip–Coating in Extreme Conditions. *J. Phys. Chem C*. **2010,** 114(17), 7637–7645.

40. Landau, L.; Levich, B. Dragging of a liquid by a moving plate, *Acta Physicochim. URSS*. **1942,** 17, 42–54.

41. Young, T. An Essay of the Cohesion of Fluids. *Philos. Trans. R. Soc. London.* **1805,** 95, 65-87.

42. Wenzel, R. N. Resistance of Solid Surfaces to Wetting by Water. *Ind. Eng. Chem.***1936,** 28, 988-994.

43. Cassie, A. B. D. Contact Angles. *Discuss. Faraday Soc.***1948,** 3, 11-16.

44. Cassie, A. B. D., Baxter, S. Wettability of Porous Surfaces. *Trans. Faraday. Soc.* **1944,** 40, 546-551.

45. Israelachvili, J. N.; Gee, M. L. Contact Angles on Chemically Heterogeneous Surfaces. *Langmuir.* **1989,** 5, 288-289.

46. Macia-Gonzalez, L.; Morrin, A.; Smyth, M. R.; Killard, A. J. Advanced printing and deposition methodologies for the fabrication of biosensors and biodevices. *Analyst,* **2010,** 135, 845–867.

47. McKinley, G. H.; Renardy, M. Wolfgang von Ohnesorge. *Phys Fluids,* **2011**, 23,127101.

48. Fromm, J. E. Numerical calculation of the fluid dynamics of drop–on–demand jets. *IBM J. Res. Dev.***1984,** 28, 322–333.

49. Jang, D.; Kim, D.; Moon, J. Influence of fluid physical properties on ink-jet printability. *Langmuir,* **2009,** 25(5), 2629-2635.

50. Meixner, R.; Cibis, D.; Krueger, K.; Goebel, H. Characterization of polymer inks for drop-on-demand printing systems. *Microsyst. Technol.* **2008**, 14(8), 1137-1142.

51. Seerden, K. A. M.; Reis, N.; Evans, J. R. G.; Grant, P. S.; Halloran, J. W.; Derby, B. Ink–Jet Printing of Wax–Based Alumina Suspensions. *J. Am. Ceram. Soc.* **2001,** 84 (11), 2514–2520.

52. Nuno, R.; Chris, A.; Brian, D. Ink–jet delivery of particle suspensions by piezoelectric droplet ejectors. *J. Appl. Phys.* **2005,** 97, 094903.

53. Gans, B. J. D.; Kazancioglu, E.; Meyer, W.; Schubert, U. S. Ink-jet Printing Polymers and Polymer Libraries Using Micropipettes. *Macromol. Rapid. Commun.* **2004,** 25(1), 292-296.

54. Izdebska, J.; Thomas, S. Printing on polymers: fundamentals and applications. **2015,** Oxford, UK.

55. Gans, B. J. D.; Duineveld, P. C.; Schubert, U. S. Inkjet Printing of Polymers: State of the Art and Future Developments. *Adv. Mater.* **2004,** 16 (3), 203–213.

56. Crowley, K.; Malley, E.; Morrin, A.; Smyth, M. R.; Killard, A. J. An aqueous ammonia sensor based on an inkjet–printed polyaniline nanoparticle–modified electrode. *Analyst,* **2008,** 133, 391–399.

57. Seung, H. K.; Jaewon, C.; Nico, H.; Koo H. N.; Costas, P. G. Metal nanoparticle direct inkjet printing for low–temperature 3D micro metal structure fabrication. *J. Micromech. Microeng.* **2010,** 20, 125010.

58. Lee, D. H.; Han, S. Y.; Herman, G. S.; Chang, C. H. Inkjet printed high–mobility indium zinc tin oxide thin film transistors. *J. Mater. Chem.* **2009,** 19, 3135–3137.

59. Singh, M.; Haverinen, H. M.; Dhagat, P.; Jabbour, G. E. Inkjet Printing–Process and Its Applications. *Adv. Mater.* **2010,** 22, 673–685.

60. Ihalainen, P.; Pesonen, M.; Sund, P.; Viitala, T.; Määttänen, A.; Sarfraz, J.; Wilén, C .E.; Österbacka, R.; Peltonen, J. Printed biotin-functionalised polythiophene films as biorecognition layers in the development of paper-based biosensors, *Appl. Surf. Sci.* **2016,** 364, 477-483.

61. Kinlen, P. J.; Liu, J.; Ding, Y.; Graham, C. R.; Remsen, E. E. Emulsion Polymerization Process for Organically Soluble and Electrically Conducting Polyaniline. *Macromolecules.* **1998,** 31, 1735-1744.

62. Owens, D. K.; Wendt, R. C.; Estimation of the surface free energy of polymers. *J. Appl. Polymer. Sci.* **1969,** 13, 1741–1747.

63. Van Oss, C. J.; Chaudhury, M. K.; Good, R. J. Monopolar surfaces. *Adv. Colloid. Inter–face Sci.* **1987,** 28, 35–64.

64. Van Oss, C. J.; Chaudhury, M. K.; Good, R. J. Interfacial Lifshitz–van der Waalsand polar interactions in macroscopic systems, *Chem. Rev.* **1988,** 88, 927–941.

65. Binnig, G.; Quate, C. F.; Gerber, C. Atomic Force Microscope. *Phys. Rev. Lett.* **1986,** 56 (9), 930–933.

66. Binnig, G.; Rohrer, H.; Gerber, C.; Weibel, E. Surface Studies by Scanning Tunneling Microscopy. *Phys. Rev. Lett.* **1982,** 49 (1), 57–61.

67. Wilson, R. A.; Bullen, H. A. Introduction to Scanning Probe Microscopy (SPM): Basic Theory Atomic Force Microscopy (AFM). Department of Chemistry, Northern Kentucky University, Highland Heights, KY 41099.

68. Guo, D.; Xie, G. X.; Luo. J. B. Mechanical properties of nanoparticles: basics and applications. *J. Phys. D: Appl. Phys.* **2014,** 47, 013001.

69. https://www.bruker.com/products/surface-analysis/atomic-force-microscopy.html

70. Markiewicz, P.; M. Cynthia, G. Atomic Force Microscopy Probe Tip Visualization and Improvement of Images Using a Simple Deconvolution Procedure. *Langmuir.* **1994,** 10, 5-7.

71. Bukharaev, A. A.; Berdunov, N. V.; Ovchinnikov, D. V.; Salikhov. K. M. Three-Dimensional Probe and Surface Reconstruction For Atomic Force Microscopy Using a Deconvolution Algorithm. *Scanning. Microscopy.* **1998,** 12(1), 225-234.

72. Canet-Ferrer, J.; Coronado, E.; Forment-Aliaga, A.; Pinilla-Cienfuegos, E.; Correction of the tip convolution effects in the imaging of nanostructures studied through scanning force microscopy. *Nanotechnology.* **2014,** 25(39), 395703.

73. Edwards, E. W.; Stoykovich, M. P.; Solak, H. H.; Nealey, P. F. Long–range order and orientation of cylinder–forming block copolymers on chemically nanopatterned striped surfaces. *Macromolecules,* **2006,** 39 (10), 3598–3607.

74. Wang, Q.; Yang, J.; Yao, W.; Wang, K.; Du, R.; Zhang, Q.; Chen, F.; Fu, Q. A simple pathway to ordered silica nanopattern from self–assembling of block copolymer containing organic silicon block. *Appl. Surf. Sci.* **2010,** 256 (20), 5843–5848.

75. Flegler, S. L.; Heckman, J. W.; Klomparens, K. L. Eds. In *Scanning and Transmission Electron Microscopy, An Introduction;* **1993,** Oxford University Press Inc. New York.

76. Lloyd, G. E. Atomic number and crystallographic contrast images with the SEM: a review of backscattered electron techniques. *Mineral. Mag.* **1987,** 51, 3–19.

77. http://www.substech.com/dokuwiki/doku.php?id=scanning_electron_microscope&s=sem

78. Järn, M. Influence of Topography and Surface Chemistry on the Wetting properties of TiO_2–based Ceramic Coatings. Doctoral thesis, **2010,** Laboratory of Physical Chemistry, Åbo Akademi University, Finland.

79. http://en.wikipedia.org/wiki/X–ray_photoelectron_spectroscopy.

80. Bragg, W. H.; Bragg, W. L. The Reflection of X–rays by Crystals. *Proc. R. Soc. Lond. A.* **1913,** 88 (605), 428–438.

81. http://ees2.geo.rpi.edu/probe/Images/concepts/concept2.html

82. Deegan, R. D.; Bakajin, O.; Dupont, T. F. ; Huber, G.; Nagel, S. R. ; Witten T. A. Capillary flow as the cause of ring stains from dried liquid drops. *Nature*. **1997,** 389, 827–829.

83. Soltman, D.; Subramanian, V. Inkjet–Printed Line Morphologies and Temperature Control of the Coffee Ring Effect. *Langmuir.* **2008,** 24(5), 2224–2231.

84. Stringer, J.; Derby, B. Formation and Stability of Lines Produced by Inkjet Printing. *Langmuir.* **2010,** 26(12), 10365–10372.

85. Nolan, N. T.; Seery, M. K.; Pillai, S. C. The Crystallisation and Phase Transition Characteristics of Sol–gel Synthesised Zinc Titanates. *Chem. Mater.* **2011,** 23, 1496–1504.

86. Bruncko, J.; Vincze, A.; Netrvalova, M.;Šutta, P.; Hasko, D.;Michalka, M. Annealing and recrystallization of amorphous ZnO thin films deposited under cryogenic conditions by pulsed laser deposition. *Thin Solid Films,* **2011,** 520 (2), 866–870.

87. Jolivet, J. P. Metal Oxide Chemistry and Synthesis: From Solution to Solid State, 3rd ed. John Wiley & Sons, **2000,** Chichester, England.

88. Soler-Illia, G. J. A. A.; Sanchez, C. Interactions between poly(ethylene oxide)-based surfactants and transition metal alkoxides: their role in the templated construction of mesostructured hybrid organic–inorganic composites. *New J. Chem.* **2000,** 24, 493-499.

89. Hanaor, D. A. H.; Sorrell, C. C. Review of the anatase to rutile phase transformation. *J. Mater. Sci.* **2011,** 46, 855–874.

90. Liu, Z.; Zhou, D.; Gong, S.; Li, H. Studies on a basic question of zinc titanates. *J. Alloys Compd.* **2009,** 475 (1), 840–845.

91. Gao, S.; Zhang, H.; Wang, X.; Deng, R.; Sun, D.; Zheng, G. ZnO–based hollow microspheres: biopolymer–assisted assemblies from ZnO nanorods. *J. Phys. Chem. B.* **2006,** 110 (32), 15847–52.

92. Kanta, A.; Sedev, R.; Ralston, J. Preparation of Silica–on–Titania Patterns with a Wettability Contrast. *Langmuir.* **2005,** 21(13), 5790–5794.

93. Tatsuma, T.; Kubo, W.; Fujishima, A. Patterning of Solid Surfaces by Photocatalytic

Lithography Based on the Remote Oxidation Effect of TiO$_2$. *Langmuir.* **2002,** 18(25), 9632–9634.

94. Lee, J. P.; Kim, H. K.; Park, C. R.; Park, G.; Kwak, H. T.; Koo, S. M.; Sung, M. M. Photocatalytic Decomposition of Alkylsiloxane Self–Assembled Monolayers on Titanium Oxide Surfaces. *J. Phys. Chem. B.* **2003,** 107(34), 8997–9002.

95. Su, S. J.; Kuramoto, N. Processable polyaniline–titanium dioxide nanocomposites: effect of titanium dioxide on the conductivity, *Synthetic. Met.* **2000,** 114, 147–153.

96. Zhou, H.; Tang, Y.; Zhai, J.; Wang, S.; Tang, Z.; Jiang, L. Enhanced photoelectrochemical detection of bioaffinity reactions by vertically oriented Au nanobranches complexed with a biotinylated polythiophene derivative. *Sensors.* **2009,** 9, 1094–1107.

97. Seto, H.; Yamashita, C.; Kamba, S.; Kondo, T.; Hasegawa ,M.; Matsuno, M.; Ogawa, Y.; Hoshino, Y.; Miura,Y. Biotinylation of silicon and nickel surfaces and detection of streptavidin as biosensor. *Langmuir.* **2013,** 29, 9457–9463.

98. Kang, E. T.; Neoh, K. G.; Tan, K. L. Polyaniline: a polymer with many interesting intrinsic redox states. *Prog. Polym. Sci.* **1998,** 23, 277–324.

99. Janata, J.; Josowicz, M. Conducting polymers in electronic chemical sensors. *Nat. Mater.* **2003,** 2, 19–24.

100. Garcia, R.; Perez, R. Dynamic atomic force microscopy methods. *Surf. Sci. Rep.* **2002,** 47, 197–301.